Impact of stoichiometry and strain on Ge1-x Snx alloys from first principles calculations

O'Donnell C.a,Sanchez-Soares A.b,Broderick C.A.a, c,Greer J.C.d

University of Nottingham
UK | CHINA | MALAYSIA

University of Nottingham Ningbo China, 199 Taikang East Road, Ningbo, 315100, China

First published 2021

This work is made available under the terms of the Creative Commons Attribution 4.0 International License:
http://creativecommons.org/licenses/by/4.0

The work is licenced to the University of Nottingham Ningbo China under the Global University Publication Licence:

https://www.nottingham.edu.cn/en/library/documents/research-support/global-university-publications-licence.pdf

University of Nottingham
UK | CHINA | MALAYSIA

Impact of stoichiometry and strain on $Ge_{1-x}Sn_x$ alloys from first principles calculations

Conor O'Donnell,[1] Alfonso Sanchez-Soares,[2] Christopher A. Broderick,[1,3,*] and James C. Greer[4,†]

[1] *Tyndall National Institute, University College Cork, Lee Maltings, Dyke Parade, Cork T12 R5CP, Ireland*
[2] *EOLAS Designs, Grenagh, Co. Cork T23 AK70, Ireland*
[3] *Department of Physics, University College Cork, Cork T12 YN60, Ireland*
[4] *Nottingham Ningbo New Materials Institute and Department of Electrical and Electronic Engineering, University of Nottingham Ningbo China, 199 Taikang East Road, Ningbo 315100, China*

(Dated: March 9, 2021)

We calculate the electronic structure of germanium-tin ($Ge_{1-x}Sn_x$) binary alloys for $0 \leq x \leq 1$ using density functional theory (DFT). Relaxed alloys with semiconducting or semimetallic behaviour as a function of Sn composition x are identified, and the impact of epitaxial strain is included by constraining supercell lattice constants perpendicular to the [001] growth direction to the lattice constants of Ge, zinc telluride (ZnTe), or cadmium telluride (CdTe) substrates. It is found that application of 1% tensile strain reduces the Sn composition required to bring the (positive) direct band gap to zero by approximately 5% compared to a relaxed $Ge_{1-x}Sn_x$ alloy having the same gap at Γ. On the other hand, compressive strain has comparatively less impact on the alloy band gap at Γ. Using DFT calculated alloy lattice and elastic constants, the critical thickness for $Ge_{1-x}Sn_x$ thin films as a function of x and substrate lattice constant is estimated, and validated against supercell DFT calculations. The analysis correctly predicts the Sn composition range at which it becomes energetically favourable for $Ge_{1-x}Sn_x$/Ge to become amorphous. The influence of stoichiometry and strain is examined in relation to reducing the magnitude of the inverted ("negative") Γ_7^--Γ_8^+ band gap, which is characteristic of semimetallic alloy electronic structure. Based on our findings, strategies for engineering the semimetal-to-semiconductor transition via strain and quantum confinement in $Ge_{1-x}Sn_x$ nanostructures are proposed.

I. INTRODUCTION

Germanium-tin ($Ge_{1-x}Sn_x$) alloys have attracted attention in recent years due to the indirect-to-direct band gap transition occurring as incorporation of Sn into Ge is increased to $x \approx 0.06 - 0.1$. The emergence of a direct band gap, combined with the reduction of the band gap energy with increasing Sn composition x, has motivated recent investigations of bulk-like $Ge_{1-x}Sn_x$,[1–4] and $Ge_{1-x}Sn_x$ nanostructures.[5] Applications of $Ge_{1-x}Sn_x$ alloys in photonic devices, including semiconductor lasers and light-emitting diodes,[6–8] and in electronic devices, including tunnelling field-effect transistors,[9–12] have been proposed and investigated. A motivation driving much of this interest is the potential for greater compatibility for on-chip photonic device integration with silicon-based microelectronics offered by use of a group-IV alloy.

Theoretical investigations have shown that the $Ge_{1-x}Sn_x$ band gap closes for Sn compositions $0.20 \lesssim x \lesssim 0.40$, with alloys at higher x being inverted-gap semimetals.[13–15] This provides motivation to study $Ge_{1-x}Sn_x$ alloys at higher Sn compositions for potential applications in novel electronic devices. Here, we consider the potential to engineer the semimetal-to-semiconductor transition in $Ge_{1-x}Sn_x$ to facilitate the formation of monomaterial Schottky-like junctions, for applications in confinement-modulated-gap electronics.[16,17] The objective is to exploit quantum confinement effects in semimetallic thin films, nanowires or two-dimensional layers to create a thick semimetallic region abutting a thin semiconducting region.[16,18–21] In the latter region, the nanostructure thickness is chosen below the length required to induce the opening of a band gap via quantum confinement, thereby allowing formation of a Schottky-like barrier within a single material.[16,22] Notably, for such a junction no impurity doping is required, thereby eliminating fabrication challenges such as dopant segregation and dopant fluctuations on the few nanometre scale, nor is there a requirement to create a heterojunction. Electronic devices can be engineered with critical dimensions just above and below the critical length for quantum confinement to create rectifying diodes from the thick/thin junction's rectifying characteristics, or transistors by gating back-to-back thick/thin junctions.[16] The thinner region becomes semiconducting due to quantum confinement. If the alloy is intrinsic, the Fermi level in this thinner region lies approximately midgap, while the thicker region remains semimetallic. The semimetallic region's work function approximately aligns to the midgap Fermi level due to the fact the two regions have similar electronegativities leading to relatively small charge transfer across the junction. Hence the conduction and valence band offsets are roughly symmetric, each being approximately equal to one-half of the magnitude of the quantum confinement-induced band gap.[22]

Diamond-structured α-Sn is a group-IV semimetal, with its crystal structure and electronic properties making it promising for electronics applications. However, the use of semimetallic α-Sn for device engineering presents two severe challenges from a practical per-

spective. The first of these is due to the structural instability of the α phase for temperatures > 13.2 °C at standard pressure, where it undergoes a phase transition to the tetragonal, metallic β phase.[23,24] Growth of lattice-matched α-Sn thin films having thicknesses up to 500 nm has been reported,[25,26] with the temperature at which the α-Sn to β-Sn phase transition occurs increasing to approximately 70°C.[25] However, this temperature is not sufficiently high for transistor operating conditions, which can exceed 100°C. Additionally, the higher phase transition temperature remains far less than temperatures required during conventional integrated circuit fabrication. A second challenge is presented by the "inverted" band structure of α-Sn,[27] which admits a large separation of > 0.5 eV between the Γ_7^- and Γ_8^+ states. This large "negative" Γ_7^--Γ_8^+ band gap must be overcome by confinement effects in a thin film or nanowire to open a band gap,[28] which is required for creating a thick/thin junction for use as a Schottky-like barrier. Furthermore, the growth of thin films is in general constrained by critical thickness limitations in the presence of substrate lattice mismatch, presenting further challenges for the growth of structurally stable α-Sn films. Here, we explore $Ge_{1-x}Sn_x$ alloys as a candidate material system to overcome these limitations in relation to confinement-modulated-gap electronic devices.[16]

The evolution of the $Ge_{1-x}Sn_x$ band gap with increasing Sn composition – from an indirect-gap semiconductor in Ge to an inverted-direct-gap semimetal in α-Sn – suggests a mechanism for engineering the length scale at which the onset of a confinement-induced semimetal-to-semiconductor transition occurs. In the absence of strain, incorporation of Ge in α-Sn reduces the magnitude of the inverted Γ_7^--Γ_8^+ energy gap. Reducing the magnitude of this negative band gap therefore relaxes constraints on nanostructure sizes required to open a band gap via quantum confinement. Predictions as to the precise nature of the inverted energy gap vary, being direct or indirect, or whether the zone-centre band ordering is topologically trivial or non-trivial.[15,29] Here, we quantify the impact of alloy composition and strain in reducing the magnitude of the negative band gap in semimetallic $Ge_{1-x}Sn_x$. Ge incorporation in α-Sn also enhances thermal lattice stability compared to α-Sn, with the potential for materials processing at higher temperatures.[25,30]

Due to the low solid solubility of Sn in Ge,[31] growth of $Ge_{1-x}Sn_x$ alloys with Sn compositions in the semimetallic range $x \gtrsim 0.20$ is challenging. Recent investigations have demonstrated that larger Sn compositions can be achieved in free-standing nanostructures due to enhanced strain relaxation relative to bulk-like epitaxial layers.[5,32–35] Sn incorporation has been demonstrated to correlate with thickness in thin film growth, with $x \approx 0.46$ achieved via growth of films having a thickness of ≈ 3 nm.[35] We have also recently quantified theoretically how miscibility can be increased via growth on lattice-matched substrates.[36] Experimentally, growth at $x \approx 0.50$ has been achieved on gallium antimonide (GaSb) substrates.[32]

Application of tensile strain has been predicted to induce an indirect- to direct-gap transition in Ge.[37–39] While application of high tensile strain can induce a semiconducting-to-semimetallic transition in Ge, the required strains – corresponding to $\approx$ 4.5% lattice-mismatch in a pseudomorphically strained, [001]-oriented epitaxial layer[39] – are sufficiently large that critical thickness limitations make this level of strain impractical. However, the results of Ref. 39 suggest that tensile strain can be exploited to reduce the Sn composition at which $Ge_{1-x}Sn_x$ becomes semimetallic. To provide a systematic analysis of the incorporation of higher Sn compositions in $Ge_{1-x}Sn_x$, and to determine the resulting impact on the electronic structure, we undertake first principles electronic structure calculations for pseudomorphically strained $Ge_{1-x}Sn_x$ as a function of both Sn composition and strain. The latter is investigated by pseudomorphically straining $Ge_{1-x}Sn_x$ alloy supercells with respect to Ge, ZnTe and CdTe substrates, with ZnTe and CdTe chosen as they respectively possess lattice constants close to that of the fictitious zinc blende IV-IV compound zb-GeSn,[40,41] and of α-Sn. To assess the feasibility of thin film growth at different strains and alloy stoichiometries, we also compute the critical thickness of pseudomorphically strained $Ge_{1-x}Sn_x$, thereby quantifying strain-related limitations to pseudomorphic growth. This allows a balance between achieving a desired electronic structure and the chosen stoichiometry and strain, while considering achievable epitaxial thin film thicknesses.

The remainder of this paper is organised as follows. In Sec. II we describe the theoretical methods employed in our analysis, focusing respectively in Secs. II A, II B, II C and II D on DFT calculations, alloy special quasi-random structures (SQSs), the impact of pseudomorphic strain on the band structure, and critical thickness limitations. Our results are presented in Sec. III, beginning in Sec. III A with our study of the evolution of the band gap of unstrained $Ge_{1-x}Sn_x$ alloys across the full alloy composition range. Sec. III B is concerned with the impact of pseudomorphic strain on the band gap evolution in $Ge_{1-x}Sn_x$ grown on Ge, ZnTe and CdTe substrates. A comparison between the strained band gaps calculated by DFT and those calculated via deformation potential theory is presented in Sec. III C, where we also describe the critical thickness of strained $Ge_{1-x}Sn_x$ grown on Ge, ZnTe or CdTe substrates, and quantify the ability to combine alloying and strain to engineer the composition at which the band gap energy becomes zero, demarcating the boundary between semiconducting and semimetallic strained alloys. Finally, in Sec. IV, we summarise and conclude.

II. METHODOLOGY

A. Electronic structure: density functional theory

Our analysis of the structural, elastic and electronic properties of $Ge_{1-x}Sn_x$ alloys is based on Kohn-Sham DFT.[42] Structural relaxations are carried out in the local density approximation (LDA).[43] Electronic band structures are calculated using the Tran-Blaha modified Becke-Johnson (TB-mBJ) meta-generalised gradient approximation (meta-GGA) exchange-correlation potential,[44] in order to overcome the band gap underestimation typical of the LDA in the Kohn-Sham formalism. Due to large relativistic effects for Sn, our electronic structure calculations include spin-orbit coupling. However, spin-orbit coupling is neglected during structural relaxations, which reduces computational time with negligible differences in the final relaxed ionic positions. Our DFT calculations employ a basis of numerical atomic orbitals (NAOs),[45–47] with a cut-off energy of 100 Ha for real-space integration. Reciprocal space integration is carried out using Γ-centred Monkhorst-Pack grids[48] with a density of ≥ 7 **k**-points / Å^{-1} along each reciprocal lattice vector. For Ge we employ a NAO basis consisting of four s, four p, three d and two f orbitals per atom ($s^4p^4d^3f^2$). We employ norm-conserving pseudopotentials in which the $(4s)^2$ and $(4p)^2$ states of Ge are treated explicitly as valence states. The semi-core $(3d)^{10}$ states of Ge are treated as core states, since unfreezing them has been demonstrated to have a minimal impact on the calculated electronic structure.[40,49] For Sn we employ a $s^4p^4d^3f^2$ NAO basis, and norm-conserving pseudopotentials in which the $(4d)^{10}$, $(5s)^2$ and $(5p)^2$ orbitals are treated explicitly as valence states. The Becke-Roussel mixing parameter c in the TB-mBJ exchange-correlation potential is treated as an adjustable parameter, and varied independently for Ge and Sn in order to accurately reproduce the overall band structure of Ge and α-Sn. We use $c_{\mathrm{Ge}} = 1.100$ and $c_{\mathrm{Sn}} = 1.225$ for our TB-mBJ calculations. The accuracy of this approach to simulate the $Ge_{1-x}Sn_x$ electronic structure has been verified recently by several groups.[15,40,49]

Figures 1(a) and 1(b) respectively show the band structure and density of states (DOS) of Ge and α-Sn calculated using this approach. Comparison of the results of our DFT calculations to experimental data and to previous calculations is provided in Table I, where we list the LDA-calculated lattice and elastic constants, as well as the TB-mBJ-calculated direct Γ_7^--Γ_8^+ and indirect L_6-Γ_8^+ band gaps, the associated hydrostatic deformation potentials $a_g(\Gamma_7^-\text{-}\Gamma_8^+)$ and $a_g(L_6^+\text{-}\Gamma_8^+)$, the valence band (VB) spin-orbit splitting energy $\Delta_0 = E(\Gamma_8^+) - E(\Gamma_7^+)$, and the VB edge axial and shear deformation potentials b and d. Where possible in Table I we compare the results of our DFT calculations to experimental measurements. We note that our LDA-calculated lattice and elastic constants slightly underestimate measured values, as expected based on the known properties of the LDA XC functional.[50] Our TB-mBJ-calculated direct and indirect band gaps are in good quantitative agreement with previous calculations and with low-temperature experimental measurements. For the hydrostatic, axial and shear deformation potentials, few experimental data are available. Here, to evaluate the accuracy of our calculated hydrostatic deformation potentials a_g we note that the corresponding, measurable band gap pressure coefficient $\frac{dE_g}{dP}$ is given by $\frac{dE_g}{dP} = -\frac{a_g}{B}$, where $B = \frac{1}{3}(C_{11} + 2C_{12})$ is the bulk modulus.[51] Using the values from Table I we respectively compute $\frac{dE_g}{dP} = 12.87$ and 4.53 meV kbar^{-1} for the pressure coefficients associated with the direct Γ_7^--Γ_8^+ and indirect (fundamental) L_6^+-Γ_8^+ band gaps of Ge. We note that these values are in excellent quantitative agreement with the recently measured values of 12.9 and 4.3 meV kbar^{-1} for Ge,[52] as well as with previous experimental measurements[53–55] and theoretical calculations.[51]

For $Ge_{1-x}Sn_x$ alloy supercell TB-mBJ calculations, we interpolate the Becke-Roussel mixing parameter c as

$$c(x) = \frac{(1-x)\,\Omega_{\mathrm{Ge}}\,c_{\mathrm{Ge}} + x\,\Omega_{\mathrm{Sn}}\,c_{\mathrm{Sn}}}{(1-x)\,\Omega_{\mathrm{Ge}} + x\,\Omega_{\mathrm{Sn}}}, \qquad (1)$$

where Ω_{Sn} and Ω_{Ge} are the equilibrium volumes of α-Sn and Ge primitive unit cells, respectively. Equation (1) therefore gives the mixing parameter by weighting c_{Ge} and c_{Sn} based on the fractional volume each element occupies in an alloy supercell at Sn composition x, thereby weighting exchange-correlation effects based upon the difference in covalent radii of Ge and Sn.

B. Strained special quasi-random supercells

Our DFT calculations are computationally demanding and therefore impose practical limits to the atomistic supercell sizes that can be employed to treat a disordered alloy such as $Ge_{1-x}Sn_x$. We therefore use the special quasi-random structure (SQS) supercell approach.[73,74] A SQS is constructed by minimising the difference between supercell lattice correlation functions and those associated with a random binary alloy, with the goal of providing a best approximation to a random alloy using a finite supercell. Our calculations employ 64-atom ($2 \times 2 \times 2$ simple cubic) $Ge_{1-x}Sn_x$ SQSs, generated stochastically using a simulated annealing procedure as implemented in the Alloy Theoretic Automated Toolkit (ATAT).[36,75] To simulate [001]-oriented $Ge_{1-x}Sn_x$ strained epitaxial layers, we apply pseudomorphic strain by (i) restricting the supercell lattice constant in the plane perpendicular to the [001] growth direction to be equal to that of a chosen substrate material, and (ii) performing structural relaxation by allowing the lattice constant along the growth direction, and the internal atomic degrees of freedom (ionic positions), to relax freely to minimise the lattice free energy.[36]

The use of SQS supercells results in (i) local relaxation of the crystal lattice, which breaks the underlying

TABLE I: DFT-calculated lattice and elastic constants, and electronic properties of Ge and α-Sn, compared to previous theoretical calculations and experimental measurements. The lattice and elastic constants a, C_{11}, C_{12} and C_{44} were computed via LDA-DFT. The direct and indirect band gaps, $E_g^{\Gamma} = E(\Gamma_7^-) - E(\Gamma_8^+)$ and $E_g^{\mathrm{L}} = E(\mathrm{L}_6^+) - E(\Gamma_8^+)$, the VB spin-orbit splitting energy $\Delta_0 = E(\Gamma_8^+) - E(\Gamma_7^+)$, the direct- and indirect-gap hydrostatic deformation potentials $a_g(\Gamma_7^-\text{-}\Gamma_8^+)$ and $a_g(\mathrm{L}_6^+\text{-}\Gamma_8^+)$, and the VB edge axial deformation potential $b(\Gamma_8^+)$ were computed via meta-GGA (TB-mBJ) DFT.

		Ge			α-Sn		
Parameter	Unit	This work	Theory	Experiment	This work	Theory	Experiment
a	Å	5.64	5.646[a]	5.657[b]	6.47	6.49[a]	6.489[c]
C_{11}	GPa	122.96	122[d], 142.5 [g]	128.53[e], 128.9[h]	68.27	68[d], 72.53[g]	69[f] 70[i]
C_{12}	GPa	49.75	47[d], 58.5[g]	48.25[e], 48.3[h]	36.59	34[d] 29.73[g]	29.3[f] 33[i]
C_{44}	GPa	60.83	86[d], 58.7[g]	66.8[e], 67.1[h]	28.98	53[d], 29.9[g]	36.2[f] 32[i]
$E(\Gamma_7^-) - E(\Gamma_8^+)$	eV	0.89	0.879[j], 0.892[m]	0.898[k]	-0.589	-0.39[j], -0.408[m], -0.64[o]	-0.413[l], -0.634[n]
$E(\mathrm{L}_6^+) - E(\Gamma_8^+)$	eV	0.78	0.71[j] 0.744[m]	0.744[k]			
$E(\Gamma_8^+) - E(\Gamma_7^+)$	eV	0.28	0.27[p] 0.3[o]	0.296[q]	0.68	0.8[o] 0.8[n]	
$a_g(\Gamma_7^-\text{-}\Gamma_8^+)$	eV	-9.54	-8.6[q]		-6.68	-9.1[q], -6.97[r]	
$a_g(\mathrm{L}_6^+\text{-}\Gamma_8^+)$	eV	-3.36	-2.78[s]		-1.53		
$b(\Gamma_8^+)$	eV	-2.78	-2.66[o] -2.16[t]		-2.39	-2.31[o]	
$d(\Gamma_8^+)$	eV	-5.95	6.06[t]		-5.23	-4.1[u]	

[a]Ref. 37 [b]Ref. 56 [c]Ref. 25,57 [d]Ref. 15 [e]Ref. 58 [f]Ref. 59 [g]Ref. 60 [h]Ref. 61 [i]Ref. 62 [j]Ref. 13 [k]Ref. 63 [l]Ref. 64 [m]Ref. 65 [n]Ref. 66 [o]Ref. 67 [p]Ref. 68 [q]Ref. 69 [r]Ref. 51 [s]Ref. 70 [t]Ref. 71 [u]Ref. 72

cubic symmetry of the diamond structure which for example would be retained in a virtual crystal approximation (VCA), and hence lifts band degeneracies present for high-symmetry points in the band structures of Ge and α-Sn,[70,76] and (ii) folding of the electronic band structures due to the reduced size of the supercell Brillouin zone compared to that associated with a primitive cubic cell of an ideal crystalline version of the alloy. These factors complicate interpretation of the alloy electronic structure.[15,40] To overcome these limitations and track the evolution of the conduction band (CB) and VB edge states in SQS supercells, we proceed by calculating overlaps between alloy states and selected states of an unperturbed Ge_{64} supercell. This approach, which is similar to the computation of the spectral function at a single **k**-point employed in popular zone unfolding schemes, enables the evolution of both the energy and character of the alloy band edge states to be identified and tracked (see, e.g., Ref. 77).

An example of this analysis is presented in Fig. 2 for a $Ge_{48}Sn_{16}$ ($x = 0.25$) SQS. The left-hand panel in Fig. 2 shows the folded supercell band structure. The right-hand panel shows the square of the eigenstate overlaps calculated by projecting the zone-centre CB edge Γ_7^-, heavy-hole (HH) and light-hole (LH) VB edge Γ_8^+, and spin-orbit split-off (SO) VB edge Γ_7^+ states of the unperturbed Ge_{64} host matrix supercell on to the full spectrum of $Ge_{48}Sn_{16}$ alloy supercell zone centre states. Here we can clearly identify (i) that the Ge Γ_7^- CB edge character resides primarily on two supercell states, reflecting Sn-induced alloy band mixing which transfers direct Ge Γ_7^- character to the hybridised alloy CB edge,[40] (ii) that the SO band edge is comparatively unperturbed for $x \approx 0.25$, reflecting that Sn incorporation tends primarily to impact the CB structure,[15,40,49] and (iii) splitting in energy and hybridisation of the LH- and HH-like VB edge states reflecting a loss of cubic symmetry due to short-range alloy disorder and associated local relaxation of the crystal lattice.[78] In the presence of pseudomorphic strain the biaxial component of the strain further reduces the lattice symmetry, acting to push HH-like (LH-like) states upwards (downwards) in energy in the presence of compressive in-plane strain, and vice-versa for tensile strain (cf. Sec. II C). Despite that short-range alloy disorder

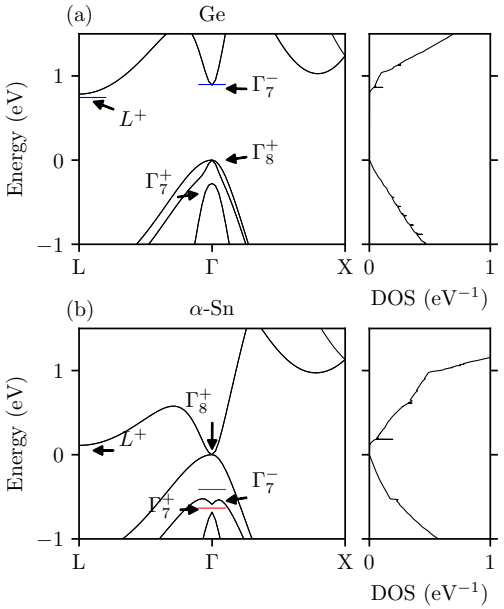

FIG. 1: DFT-calculated band structure (left-hand panel) and DOS (right-hand panel) of (a) Ge, and (b) α-Sn. The zero of energy is chosen to lie at the Fermi energy. Note the inverted ordering of the Γ_8^+ and Γ_7^- states for Sn relative to Ge. In (a) the solid blue lines denote the measured low-temperature indirect (fundamental) L_6^+-Γ_8^+ and direct Γ_7^--Γ_8^+ band gaps of Ge.[63] In (b) the solid green and red lines denote the measured low temperature Γ_8^+-Γ_7^- (inverted band gap) energy in α-Sn.[64,66]

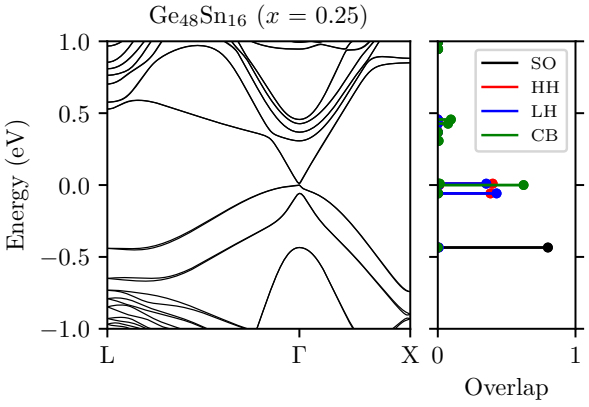

FIG. 2: Left-hand panel: meta-GGA DFT-calculated band structure of a $Ge_{48}Sn_{16}$ ($x = 0.25$) SQS. Right-hand panel: calculated squared overlaps between the alloy SQS zone centre states and the SO (Γ_7^-, solid black lines), HH (Γ_8^+, solid red lines), LH (Γ_8^+, solid blue lines), and CB (Γ_7^-, solid green lines) states of a Ge_{64} supercell.

drives hybridisation between HH- and LH-like VB states we find generally, as expected for a diamond-like semiconductor, that the state at the alloy Fermi level possesses more Ge HH (LH) Γ_8^+ character in the presence of compressive (tensile) in-plane strain (cf. Eqs. (3) and (4)).

The presence of reduced lattice symmetry and alloy-induced hybridisation complicates interpretation of the alloy electronic structure. Generally, no single alloy supercell state possesses, e.g., 100% Γ_7^- or Γ_8^+ character.[40,79] To identify the corresponding energy difference between the two bands Γ_7^--Γ_8^+ in our SQS calculations, we select the lowest energy supercell state possessing appreciable Ge Γ_7^- character, and the highest energy supercell state possessing appreciable Ge Γ_8^+ character. In the case of semiconducting $Ge_{1-x}Sn_x$ ($x \lesssim 0.20$) this defines the direct band gap at the Brillouin zone centre, while for higher Sn compositions it defines the maximum inverted (negative) energy gap that must be overcome by quantum confinement to open a band gap in a semimetallic alloy. For reference, calculated supercell band structures and overlaps for relaxed and pseudomorphically strained $Ge_{1-x}Sn_x$ SQSs are provided as Supplementary Information.

C. Deformation potential theory

To aid interpretation of our alloy supercell electronic structure calculations, we apply a deformation potential theory approach.[70,76] We compare the variation of the strain-dependent alloy supercell Γ_7^- zone-centre CB edge energy, as well as the Γ_8^+ HH, Γ_8^+ LH, and Γ_7^+ SO VB edge energies computed via deformation potential theory to those obtained directly from our TB-mBJ DFT calculations. This comparison also highlights deviations from idealised behaviour associated with alloy band hybridisation effects and short-range alloy disorder.[15,40,52]

Pseudomorphic strain in an [001]-oriented cubic crystal results in strain-related shifts to the CB and VB edge energies. The pseudomorphic strain-related shifts to the zone-centre energy of band n = CB, VB are described by a purely diagonal strain tensor and consist of a distinct (i) hydrostatic contribution $\delta E_{\mathrm{hy},n}$, and (ii) biaxial contribution $\delta E_{\mathrm{ax},n}$, which are respectively associated with (i) a change in unit cell volume that is directly proportional to the trace of the strain tensor $\mathrm{Tr}(\epsilon) = \epsilon_{xx} + \epsilon_{yy} + \epsilon_{zz}$, and (ii) the biaxial component of the strain tensor $\epsilon_b = \epsilon_{zz} - \frac{1}{2}(\epsilon_{xx} + \epsilon_{yy})$, which describes the lattice relaxation along the growth direction in response to the in-plane strain imposed via growth on a substrate. Biaxial strain breaks the underlying cubic symmetry of the lattice, lifting the degeneracy of the p-like Γ_8^+ HH and LH VB edge states.[70,76] The hydrostatic and biaxial energy shifts are given by $\delta E_{\mathrm{hy},n} = a_n \mathrm{Tr}(\epsilon)$ and $\delta E_{\mathrm{ax},n} = b_n \epsilon_b$, where a_n and b_n are, respectively, the hydrostatic and axial deformation potentials associated with band n. We denote the CB edge Γ_7^- and VB edge Γ_8^+ hydrostatic deformation potentials by a_c and a_v, respectively. The s-like Γ_7^- zone-centre CB edge is not impacted by biaxial strain, so that $b_{\mathrm{CB}} = 0$. We denote

the (non-zero) VB edge axial deformation potential by $b_{\rm VB} = b(\Gamma_8^+)$ (cf. Table I).

Taking the zero of energy to lie at the unstrained VB edge, the strain-dependent Γ-point CB, HH, LH and SO band edge energies in an [001]-oriented pseudomorphic strained layer are given respectively by[70,76]

$$E_{\rm CB} = E_g + a_c {\rm Tr}\left(\epsilon\right) , \quad (2)$$

$$E_{\rm HH} = a_v {\rm Tr}\left(\epsilon\right) - \delta E_{\rm ax,VB} , \quad (3)$$

$$E_{\rm LH} = a_v {\rm Tr}\left(\epsilon\right) - \frac{1}{2}\left(\Delta_0 + \delta E_{\rm ax,VB}\right) + \frac{1}{2}\sqrt{\Delta_0^2 + 2\Delta_0 \delta E_{\rm ax,VB} + 9\left(\delta E_{\rm ax,VB}\right)^2} , \quad (4)$$

$$E_{\rm SO} = a_v {\rm Tr}\left(\epsilon\right) - \frac{1}{2}\left(\Delta_0 - \delta E_{\rm ax,VB}\right) - \frac{1}{2}\sqrt{\Delta_0^2 + 2\Delta_0 \delta E_{\rm ax,VB} + 9\left(\delta E_{\rm ax,VB}\right)^2} , \quad (5)$$

where $E_g = E(\Gamma_7^-) - E(\Gamma_8^+)$ and $\Delta_0 = E(\Gamma_8^+) - E(\Gamma_7^+)$ are, respectively, the direct band gap and VB spin-orbit splitting energy of the unstrained material (cf. Table I). In the absence of strain, Eqs. (2) – (5) yield $E_{\rm CB} = E_g$, $E_{\rm HH} = E_{\rm LH} = 0$, and $E_{\rm SO} = -\Delta_0$. In the presence of compressive (tensile) strain, corresponding here to $\epsilon_{xx} < 0$ ($\epsilon_{xx} > 0$), we have $E_{\rm HH} > E_{\rm LH}$ ($E_{\rm HH} < E_{\rm LH}$).

Choosing the z-axis to align to the growth direction, for a [001]-oriented pseudomorphic layer we have $\epsilon_{xx} = \epsilon_{yy} = \frac{a_{\rm S} - a_{\rm L}}{a_{\rm L}}$ as the fractional lattice mismatch in the plane perpendicular to the growth direction due to lattice mismatch between the layer having lattice constant $a_{\rm L}$, and the substrate having lattice constant $a_{\rm S}$. Similarly, $\epsilon_{zz} = -\frac{2C_{12}}{C_{11}}\epsilon_{xx}$ describes the corresponding relaxation of the layer along the growth direction in response to the in-plane strain.[70,76] As such, ${\rm Tr}(\epsilon) = 2(1 - \frac{C_{12}}{C_{11}})\epsilon_{xx}$ and $\epsilon_b = -(1 + \frac{2C_{12}}{C_{11}})\epsilon_{xx}$. Under hydrostatic strain, $\epsilon_{xx} = \epsilon_{yy} = \epsilon_{zz}$, the strain-induced change in band gap is given via Eqs. (2) and (3) as $a_g {\rm Tr}(\epsilon)$, where $a_g = a_c - a_v$ is the direct-gap hydrostatic deformation potential (i.e. $a_g(\Gamma_7^-$-$\Gamma_8^+)$; cf. Table I), related to the band gap pressure coefficient as $\frac{dE_g}{dP} = -\frac{a_g}{B}$ (cf. Sec. II A).

To evaluate Eqs. (2) – (5) we have computed the elastic constants and CB and VB edge deformation potentials for Ge and α-Sn directly via TB-mBJ DFT (cf. Table I). The hydrostatic band gap deformation potentials a_g were obtained by calculating the direct and indirect energy gaps Γ_7^--Γ_8^+ and L_6^+-Γ_8^+ for Ge and α-Sn under applied hydrostatic pressure. The VB edge axial deformation potentials b were obtained by calculating the splitting between the HH and LH VB edge energies under an applied volume-preserving (to first order in ϵ) uniaxial strain along [001]. To analyse our $Ge_{1-x}Sn_x$ alloy SQS calculations, we linearly interpolate the deformation potentials of Ge and α-Sn to obtain deformation potentials for $Ge_{1-x}Sn_x$, and also consider best-fit deformation potentials which reflect alloy-induced hybridisation between distinct host matrix eigenstates (cf. Sec. III C). The elastic constants used in our calculations were computed via LDA DFT for Ge and α-Sn via stress tensors computed under applied high-symmetry strain branches.[41,80] For completeness, we list also in Table I the elastic constant C_{44} and VB edge shear deformation potential d, which do not enter into the present analysis. Repeating the elastic constant calculations for the $Ge_{1-x}Sn_x$ alloy SQSs, we find significant bowing of the elastic constants. The bowing parameters for C_{11}, C_{12} and C_{44} were respectively computed as 40.87, 4.82 and 30.41 GPa, and were used to interpolate the elastic constants used in our calculation of the components of the strain tensor via Eqs. (2) – (5), and also in our critical thickness calculations below.

D. Critical thickness

The growth of pseudomorphically strained layers proceeds for layer thicknesses $t \lesssim t_c$, beyond which plastic relaxation via the formation of dislocations and related crystalline defects becomes energetically favourable.[81] For a pseudomorphically strained layer this critical thickness t_c can be computed as the root of the intrinsic equation[82]

$$t_c = \frac{a_{\rm S}}{8\sqrt{2}\pi|\epsilon_{xx}|}\left(\frac{4-\sigma}{1+\sigma}\right)\left(1 + \ln\left(\frac{\sqrt{2}t_c}{a_{\rm S}}\right)\right) , \quad (6)$$

where $a_{\rm S}$ is the substrate lattice constant, ϵ_{xx} is the lattice mismatch between the substrate and the layer in the plane perpendicular to the [001] direction, and $\sigma = \frac{C_{12}}{C_{11}+C_{12}}$ is Poisson's ratio for the layer. While there exist numerous approaches to compute t_c,[81] Eq. (6) has been demonstrated to produce estimates which are in good agreement with experimental measurements for a range of semiconductor materials, including group-IV Si_xGe_{1-x} and III-V $In_yGa_{1-y}As$ alloys,[81,82] as well as highly-mismatched III-V alloys containing nitrogen or bismuth.[83,84] As we describe in Sec. III C below, the estimates of t_c computed via Eq. (6) are in quantitative agreement with the results of LDA DFT structural relaxation for disordered $Ge_{1-x}Sn_x$ alloy supercells.

III. RESULTS

We next consider the results of our calculations, and analysis of the band gap and semimetal to semiconductor transition in $Ge_{1-x}Sn_x$. In Secs. III A and III B we analyse the electronic structure of relaxed and pseudomorphically strained alloys. In Sec. III C, we compare the results of our strained alloy supercell DFT calculations to the deformation potential theory of Sec. II C, analyse critical thickness limitations associated with growth of $Ge_{1-x}Sn_x$ on Ge, ZnTe and CdTe substrates, and explore the effects of tensile strain to reduce the Sn composition required to close the band gap and achieve a semimetallic band structure in pseudomorphic $Ge_{1-x}Sn_x$.

A. Band gap evolution in relaxed $Ge_{1-x}Sn_x$ alloys

Ge possesses an indirect fundamental band gap between the L_6^+ CB minimum and Γ_8^+ VB maximum, while α-Sn possesses a direct inverted band gap between the Γ_7^- and Γ_8^+ zone-centre eigenstates. Being an inverted-gap semimetal, α-Sn has no band gap above the Γ_8^+ VB edge, but does display a vanishing DOS where the VB and CB meet (i.e. at the Fermi energy). It has been demonstrated theoretically that quantum confinement effects can be exploited to open a direct band gap in α-Sn thin films or nanowires, by pushing the s-like Γ_7^- states higher in energy than the p-like Γ_8^+ states.[28] As an example of this behaviour, we present in Fig. 3 the LDA DFT-calculated orbital resolved band structure of a 1.3 nm thick, [001]-oriented and hydrogen (H) passivated α-Sn thin film. The thin film supercell is constructed using a $1 \times 1 \times 2$ simple cubic α-Sn unit cell, with the dangling bonds on the upper and lower (001) planes passivated using H atoms, above which along [001] is placed 1.5 nm of vacuum. With periodic (Born-von Kármán) boundary conditions applied, the film is continuous in the (001) plane, with adjacent films along the [001] direction separated by a 1.5 nm vacuum region. The black solid lines show the calculated energy bands of this thin film in the (001) plane, demonstrating the opening of a direct band gap above the Fermi level, chosen in Fig. 3 to lie at the zero of energy. The weighted green and red colour of the overlaid circles respectively denote the total s and p orbital character of the associated band states. Examining the orbital character, we note that the zone-centre CB minimum is purely s-like, reflecting that it originates from an upward shift in energy of the Γ_7^- states of α-Sn in response to quantum confinement. We note that the TB-mBJ exchange-correlation potential applied in our analysis of bulk-like $Ge_{1-x}Sn_x$ supercells is not applicable in thin film calculations, as the potential becomes singular in the presence of vanishing charge density.[44] The LDA-calculated 219 meV band gap in Fig. 3 is therefore likely underestimated,[85] but nonetheless, as a known underestimate of the band gap energy, strongly suggests that a direct band gap can be opened in α-Sn thin films via quantum confinement.

Previous theoretical calculations have predicted the evolution and nature of the $Ge_{1-x}Sn_x$ alloy band gap across the full composition range, from Ge to α-Sn.[13,15,29] Beginning with the indirect-gap semiconductor Ge, Sn incorporation drives rapid band gap reduction and an indirect to direct-gap transition for $x \lesssim 0.10$. Beyond this composition, the direct band gap decreases in magnitude until it closes between $0.2 \lesssim x \lesssim 0.4$, at which point the alloy becomes a zero-gap semimetal. For higher Sn compositions the alloy band structure is predicted to be semimetallic and possesses an inverted Γ_7^--Γ_8^+ band ordering. We have firstly employed TB-mBJ DFT calculations to verify the evolution of the $Ge_{1-x}Sn_x$ band gap using relaxed 64-atom SQSs. The results of these calculations are summarised in Fig. 4, where closed red

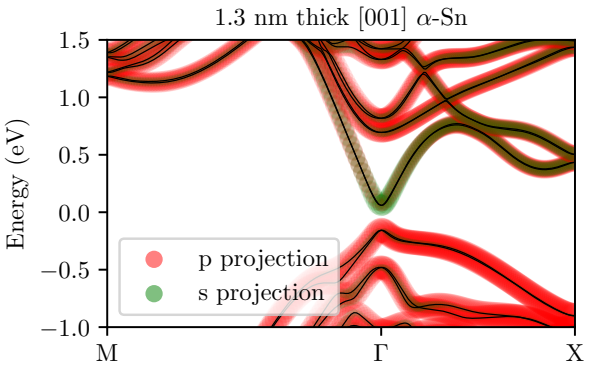

FIG. 3: Opening of a direct band gap via quantum confinement in a semimetallic α-Sn thin film: s (red) and p (green) orbital resolved band structure of an (001)-oriented, H-passivated film of thickness 1.3 nm calculated via LDA-DFT.

circles denote the calculated fundamental alloy band gap. The solid black line shows the corresponding fundamental band gap calculated via a cluster expansion approach,[86] allowing for prediction of alloy properties as the SQS lattice correlation functions approximate those of a random alloy. We note that the cluster expansion approach has been recently applied to quantify the formation enthalpy and alloy miscibility in $Ge_{1-x}Sn_x$.[36] The dashed black line in Fig. 4 denotes the composition at which a zero band gap is predicted to occur thereby demarcating the Sn compositions at which the alloy is either semiconducting or semimetallic. Negative values refer to the inverted (semimetallic) Γ_7^--Γ_8^+ energy gaps.

At low Sn compositions $x \lesssim 0.20$, we calculate a rapid band gap reduction with increasing x (the indirect- to direct-gap transition occurring in this composition range is discussed in Sec. III C). Our calculated band gaps are also compared to experimental measurements in Fig. 4. Generally, $Ge_{1-x}Sn_x$ is grown as a thin strained, or thick relaxed, epitaxial layer on a substrate having a lattice constant close to that of Ge. The resultant pseudomorphic strain complicates the comparison between calculated and measured band gaps, due to the impact of strain on the magnitude of the band gap (cf. Sec. II C). In Fig. 4, we therefore compare the results of our TB-mBJ DFT calculations to experimental data in which the impact of pseudomorphic strain is minimised. Specifically, we compare our calculations to the results of photo-modulated reflectance (Ref. 87; open green triangles) and optical absorption (Refs. 88 and 89; open pink triangles and blue squares, respectively) spectroscopic measurements. The photo-modulated reflectance measurements of Ref. 87 were performed on epitaxial layers grown on nominally lattice-matched $In_yGa_{1-y}As$ buffer layers, thereby minimising strain. The absorption measurements of Ref. 88 were performed on strained $Ge_{1-x}Sn_x$ epitaxial layers, but the data were then corrected to account for the strain-induced effects on the band gap,

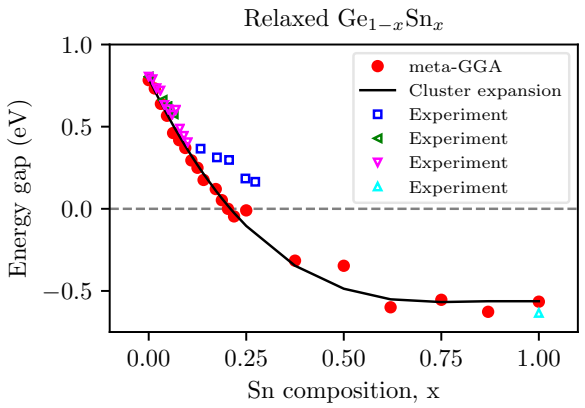

FIG. 4: Meta-GGA DFT-calculated band gap as a function of Sn composition x of $Ge_{1-x}Sn_x$ alloy SQSs across the full alloy composition range. The solid black line represents the corresponding cluster expansion calculation. Closed green triangles, pink triangles and blue squares denote measured low temperature band gaps in the semiconducting regime,[87–89] and the light blue triangle denotes the experimentally measured inverted gap of α-Sn[64]. The horizontal dashed line denotes zero band gap, demarcating between semiconducting and semimetallic band structure.

based on strain values extracted from x-ray diffraction measurements. The absorption measurements of Ref. 89 were performed on thick, relaxed epitaxial layers grown on Si substrates. We note excellent quantitative agreement between our calculated band gap as a function of Sn composition x and that measured by Lin et al.[87] and by Tran et al.[88]. However, our calculations deviate from the measurements of Xu et al.[89] for $0.15 \lesssim x \lesssim 0.25$. Given the large lattice mismatch between $Ge_{1-x}Sn_x$ and the Si substrates employed by Xu et al.[89], it is possible that there remains residual compressive strain associated with partial relaxation in their samples which would act to increase the band gap, possibly explaining why our calculations underestimate those measured band gaps. Finally, the open light-blue triangle represents the α-Sn inverted direct Γ_7^--Γ_8^+ energy gap, measured by Booth and Ewald[64] via magnetoresistance (cf. Table I). Overall, we note good quantitative agreement between our theoretical calculations and comparable experimental data.

We predict a closing of the band gap in relaxed $Ge_{1-x}Sn_x$ for $x \approx 0.21$. Analysis of the supercell electronic structure for SQSs having $x \gtrsim 0.21$ reveals that the alloy is semimetallic, in agreement with recent theoretical calculations.[15,29] For Sn compositions $x \gtrsim 0.50$, we predict that the magnitude of the inverted Γ_7^--Γ_8^+ energy gap remains close to the value -0.59 eV calculated for α-Sn (cf. Table I). There are, however, differing predictions in the literature regarding the precise nature of the semimetallic alloy band structure for $x \gtrsim 0.20$. Using empirical pseudopotential calculations in the virtual crystal approximation, Lan et al.[29] predicted that the band ordering remains topologically non-trivial in this composition range with Γ_7^- states lying lower and higher in energy than Γ_8^+ and Γ_7^+ states, respectively. Conversely, by applying zone unfolding to DFT calculations for SQS supercells, Polak et al.[15] predicted the presence of a topologically trivial "inverted SO" band structure for $0.45 \lesssim x \lesssim 0.85$, in which the Γ_7^- states drop lower in energy than the Γ_7^+ states. However, it is noteworthy that the quadratic composition dependent band gap fit applied by Polak et al.[15] to extract this conclusion is poorer in quality for $x \gtrsim 0.30$ compared to its accuracy at lower Sn compositions.

To resolve these contrasting predictions, we have undertaken a direct analysis of the alloy supercell zone-centre states, via projection onto reference Γ_7^-, Γ_8^+ and Γ_7^+ states calculated for a Ge_{64} supercell (cf. Fig. 2). Applying this quantitative approach, we find that the alloy state retaining the largest calculated Γ_7^- character reduces in energy with increasing x, approaching the state retaining the largest calculated Γ_7^+ character. At $x = 0.625$ ($Ge_{24}Sn_{40}$ SQS), we calculate that these Ge Γ_7^-- and Γ_7^+-derived alloy states become quasi-degenerate, and remain so for Sn compositions up to $x = 0.875$ (corresponding to a Ge_8Sn_{56} SQS), beyond which composition the relative energy of the Ge Γ_7^--derived alloy state increases to reach its value in α-Sn – i.e. lying ≈ 100 meV above Γ_7^+ in energy (cf. Table I). In only one of the supercells analysed was a Ge Γ_7^--derived alloy state found to lie lower in energy than a Γ_7^+-derived state, and in that case only by 10 meV and with additional Ge Γ_7^- character residing on higher energy alloy states. Our calculations therefore suggest that semimetallic $Ge_{1-x}Sn_x$ most likely retains topologically non-trivial band ordering for $0.21 \lesssim x \leq 1$, but we note that the specific band ordering close to $x = 0.60$ for small supercell calculations is determined in part by the impact of alloy-induced band hybridisation, arising due to the precise reduction in symmetry associated with the specific alloy disorder and lattice relaxation present in a given alloy SQS.

We attribute deviations between previous predictions to the simplified manner in which the alloy band structure was analysed, generally based on either (i) assuming virtual crystal-like behaviour and simple polynomial fits to composition-dependent band gaps obtained from theoretical data, or (ii) extrapolation of low x experimental data across the full composition range. In particular, large uncertainties associated with extrapolation of experimental data have produced divergent predictions,[89] including (i) that the magnitude of the inverted Γ_7^--Γ_8^+ alloy energy gap exceeds that of α-Sn by up to 0.2 eV, or (ii) that the direct Γ_7^--Γ_8^+ band gap remains open with a constant magnitude ≈ 0.1 eV up to $x \approx 0.70$. We emphasise that our conclusions here are based on direct investigation of the character and evolution of hybridised alloy supercell eigenstates calculated from first principles.

Our calculations indicate that the magnitude of the direct inverted band gap in relaxed $Ge_{1-x}Sn_x$ can be tuned between zero and close to that of α-Sn for $0.21 \lesssim x \lesssim$

0.50. This provides the ability to reduce the magnitude of the inverted Γ_7^--Γ_8^+ energy gap that must be overcome to open a band gap via quantum confinement. Alloying therefore provides a degree of freedom in addition to nanostructuring, which can be utilised to engineer a semimetal-to-semiconductor transition via quantum confinement. In what follows, we turn our attention to the band structure of pseudomorphically strained $Ge_{1-x}Sn_x$ alloys, on which basis we then quantify the impact of alloying and strain in epitaxial thin films, in order to provide further control over the inverted energy gap and hence the semimetal-to-semiconductor transition.

B. Band structure evolution in pseudomorphically strained $Ge_{1-x}Sn_x$

Having analysed the nature and evolution of the $Ge_{1-x}Sn_x$ band gap for the full composition range in relaxed alloys, we now consider pseudomorphically strained $Ge_{1-x}Sn_x$ grown on (i) Ge, (ii) ZnTe, and (iii) CdTe substrates. ZnTe and CdTe have lattice constants close to those calculated for zb-GeSn[40,41] and α-Sn, respectively. For each substrate, we take the SQSs of Sec. III A and simulate [001]-oriented pseudomorphically strained $Ge_{1-x}Sn_x$ by fixing the supercell lattice constants along the [100] and [010] directions to mimic the substrate lattice constant. Next, we perform a LDA relaxation of the [001] lattice supercell parameter and all ionic positions. We then perform a TB-mBJ electronic structure calculation for these pseudmorphically strained SQSs, and again quantify the character of the alloy supercell eigenstates by projecting them onto reference states from a Ge_{64} supercell. On this basis we assign a Γ_7^--Γ_8^+ energy gap for each strained SQS, as above.

The results of these calculations are summarised in Fig. 5, where the closed red circles repeat the results of the unstrained calculations of Fig. 4 for reference. The closed light blue triangles, closed green triangles and closed blue squares in Fig. 5 respectively show the calculated variation of the Γ_7^--Γ_8^+ energy difference (direct band gap) across the full composition range for $Ge_{1-x}Sn_x$ alloys pseudomorphically strained to [001]-oriented Ge, ZnTe and CdTe substrates. Our LDA total energy calculations suggest that, when grown on Ge, it is energetically favourable for $Ge_{1-x}Sn_x$ to become amorphous for Sn compositions $x \gtrsim 0.56$.[36] Interpolating the LDA-calculated Ge and α-Sn lattice constants of Table I using a bowing parameter of 0.056 Å,[36] $x = 0.56$ corresponds to a (compressive) lattice mismatch $\epsilon_{xx} \approx -7.8\%$. As such, the associated $Ge_{1-x}Sn_x$/Ge band gap is shown only up to $x = 0.5$ in Fig. 5 (light blue triangles). As we will describe in Sec. III C, this conclusion is in quantitative agreement with our estimation of the $Ge_{1-x}Sn_x$/Ge critical thickness.

Comparing the band gaps of relaxed $Ge_{1-x}Sn_x$ and compressively strained $Ge_{1-x}Sn_x$/Ge in Fig. 5, we note that the latter closely track the former for $x \lesssim 0.30$.

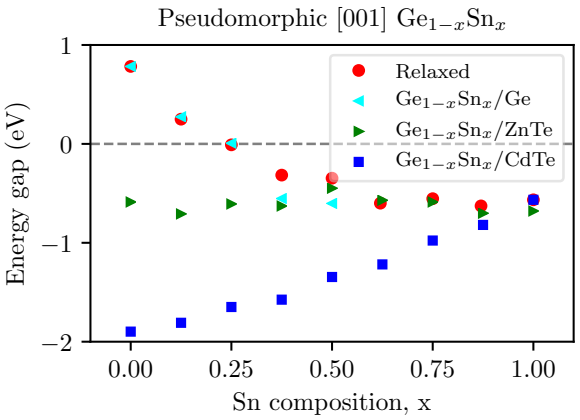

FIG. 5: Meta-GGA DFT-calculated band gap as a function of Sn composition x of $Ge_{1-x}Sn_x$ alloy SQSs which are freely relaxed (closed red circles), or pseudomorphically strained and internally relaxed to correspond to growth on Ge (closed light blue triangles), ZnTe (closed green triangles), or CdTe (closed blue squares) substrates. The horizontal dashed line denotes zero band gap, demarcating between semiconducting and semimetallic band structure.

The strained $Ge_{1-x}Sn_x$/Ge band gaps are calculated to slightly exceed those of relaxed $Ge_{1-x}Sn_x$ in this composition range, reflecting that compressive pseudomorphic strain acts to slightly increase the band gap (cf. Eqs. (2) – (4)). As the Sn composition is increased above $x = 0.30$, we note that the calculated magnitude of the inverted (negative) Γ_7^--Γ_8^+ energy gap of strained $Ge_{1-x}Sn_x$/Ge exceeds that in relaxed $Ge_{1-x}Sn_x$, i.e. the Ge Γ_7^--derived alloy state is lower in energy relative to the Ge Γ_8^+-derived state that corresponds to the alloy VB edge. This is contrary to the expected trend based on the compressive strain in the $Ge_{1-x}Sn_x$/Ge SQSs within this composition range. Based on our analysis of the character of the eigenstates for the corresponding SQSs (cf. Supplementary Information), we attribute this behaviour to alloy-induced hybridisation which distributes the Ge Γ_7^- character over an energy range $\lesssim 1$ eV in width. If instead of assigning as Γ_7^- the lowest energy alloy state possessing appreciable Ge Γ_7^-, as described in Sec. II B, the weighted average energy of the supercell eigenstates is instead calculated – using the computed Ge Γ_7^- character of each state as the weight for that state's energy – this trend is reversed, and leads to $Ge_{1-x}Sn_x$/Ge inverted band gaps which are smaller in magnitude than in relaxed $Ge_{1-x}Sn_x$, as expected for compressive strain.

Next, we note that the inverted band gap in tensile strained $Ge_{1-x}Sn_x$/CdTe, shown using closed blue squares in Fig. 5, increases in magnitude as Ge is incorporated into α-Sn. This behaviour is in line with the expected reduction in energy of Γ_7^- states relative to Γ_8^+ states in the presence of tensile in-plane strain (cf. Eqs. (2) and (4)). Our calculated energy gaps for $Ge_{1-x}Sn_x$/CdTe therefore suggest that growth of tensile strained $Ge_{1-x}Sn_x$ will increase the magnitude of the in-

verted Γ_7^--Γ_8^+ energy gap, making it challenging to for an energy band gap to be opened via quantum confinement in a nanostructure.

Considering $Ge_{1-x}Sn_x$/ZnTe (closed green triangles in Fig. 5), the substrate introduces compressive (tensile) in-plane strain for $x \geq 0.54$ ($x \leq 0.54$). In both cases, we note that the magnitude of the inverted Γ_7^--Γ_8^+ energy gap remains approximately constant independent of changes in Sn composition. Reducing the Sn composition from $x = 0.54$ results in tensile in-plane strain. In this composition range, a reduction in x acts to increase the energy of Γ_7^--like states relative to Γ_8^+-like states, resulting in a reduction of the magnitude of the inverted band gap. Due to the strain present in pseudomorphic $Ge_{1-x}Sn_x$/ZnTe, the composition-dependent band edge energy shifts are counteracted by the tensile in-plane strain which acts to decrease (increase) the energy of Γ_7^--like (LH Γ_8^+-like) states. This competition between Sn composition and strain is mirrored in the compressively strained regime, leading to a $Ge_{1-x}Sn_x$/ZnTe inverted energy gap which remains relatively constant across the full composition range. We note that the calculated 448 meV magnitude of the inverted band gap in approximately lattice-matched $Ge_{0.5}Sn_{0.5}$ ($Ge_{32}Sn_{32}$ SQS) is approximately two-thirds of the magnitude of the inverted Γ_7^--Γ_8^+ energy gap of α-Sn. An equivalent TB-mBJ band structure calculation predicts that zb-GeSn (i.e. an ordered $Ge_{0.5}Sn_{0.5}$ alloy) is a zero-gap semiconductor,[40] with the significant difference in band gap between ordered zb-GeSn and disordered $Ge_{0.5}Sn_{0.5}$ highlighting that, at fixed Sn composition, the magnitude of the inverted energy gap is strongly influenced by short-range alloy disorder.[40]

The magnitude of the inverted band gap shown in Fig. 5 for $Ge_{1-x}Sn_x$/ZnTe is (i) associated with maximally random alloy disorder due to the use of SQSs in our calculations, and (ii) explicitly assigned the largest possible value, via our previously described explicit assignment of the lowest energy alloy state possessing appreciable Ge Γ_7^- character as "Γ_7^-" in our energy gap calculations (cf. Sec. II B). As such, the magnitude of the inverted band gap in $Ge_{1-x}Sn_x$/ZnTe indicated in Fig. 5 should be considered an upper limit, which is likely reduced both in a real alloy (where more states are free to hybridise than in the small supercell calculations considered here, leading to less energetic spread of Ge Γ_7^- character), and in the presence of partial alloy ordering (where the inverted band gap is expected to move towards the zero band gap of ordered zb-GeSn). In addition to alloying, strain is seen to provide another degree of freedom that can be exploited to engineer the electronic structure in $Ge_{1-x}Sn_x$ to be either semimetallic or semiconducting. Choosing a substrate and alloy composition determines the magnitude of the inverted Γ_7^--Γ_8^+ energy gap that needs to be overcome to achieve a semimetal-to-semiconductor transition driven by quantum confinement.

C. Engineering the electronic structure of pseudomorphic $Ge_{1-x}Sn_x$

We next consider the impact of strain on the band gap using deformation potential theory, and describe trends in light of the results of our DFT alloy SQS calculations. This provides an efficient means by which to predict strain-dependent energy gaps, while also providing qualitative insight into alloy-induced band mixing effects. We then predict critical thickness limitations for $Ge_{1-x}Sn_x$ alloys grown on Ge, ZnTe and CdTe substrates. Finally, we describe the alloy composition and strain for determining whether a given bulk alloy will be semiconducting or semimetallic, and provide general recommendations for the growth of pseudomorphically strained $Ge_{1-x}Sn_x$ thin films in which the band gap is closed within known alloy miscibility restrictions – i.e. at the lowest possible Sn composition, and within critical thickness limits.

We begin our deformation potential theory analysis by considering the band gap of pseudomorphically strained Ge and α-Sn. The results of these calculations are summarised in Figs. 6(a) and 6(b), respectively. In each case, closed green circles show the TB-mBJ DFT-calculated direct Γ_7^--Γ_8^+ energy gap, as a function of in-plane strain ϵ_{xx}. We note that in-plane strain values < 0 (> 0) correspond to compressive (tensile) strain (cf. Sec. II C). Closed red circles in Figs. 6(a) and 6(b) show the TB-mBJ DFT-calculated indirect L_6^+-Γ_8^+ energy gap. Green and red lines in Figs. 6(a) and 6(b) respectively show the corresponding energy gaps calculated via Eqs. (2) – (4), using the parameters listed in Table I. Solid and dashed lines respectively show the band gaps calculated with respect to HH- and LH-like Γ_8^+ VB states, where we recall that $E_{\rm HH} > E_{\rm LH}$ for $\epsilon_{xx} < 0$ (and vice versa), so that solid (dashed) lines represent the direct Γ_7^--Γ_8^+ and indirect L_6^+-Γ_8^+ band gaps associated with HH- (LH-) like Γ_8^+ VB edge states in the compressive (tensile) strained regime. Closed blue triangles in Fig. 6(a) show experimental measurements of the direct band gap of tensile-strained Ge epitaxial layers.[90] We note in Figs. 6(a) and 6(b) good quantitative agreement between the full DFT (circles) and deformation potential theory (lines) calculations. We attribute increased deviation between the DFT-calculated and deformation potential theory results at high compressive strain in Ge to increasing non-linear strain contributions, which are not captured by Eqs. (2) – (4). The experimental measurements of the strain-dependent Ge direct band gap of Ref. 90 were performed at room temperature. In order to compare these data to our zero-temperature DFT calculations, we have applied a rigid energy shift to the experimental data so that the measured and calculated direct band gaps coincide at zero strain. We then note excellent quantitative agreement between theory and experiment, with our DFT-based deformation potential theory calculations quantitatively describing the tensile strain-induced reduction of the direct band gap.

For pristine Ge, our calculations predict that pseudo-

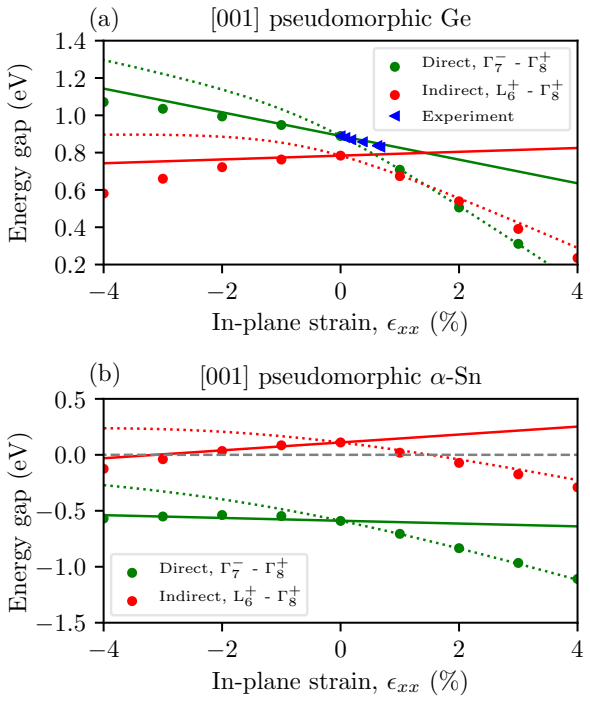

FIG. 6: (a) Meta-GGA DFT-calculated indirect (L_6^+-Γ_8^+; closed red circles) and direct (Γ_7^--Γ_8^+; closed green circles) band gaps of pseudmorphically strained (a) Ge, and (b) α-Sn, as a function of in-plane strain ϵ_{xx}. Solid and dashed lines show band gaps calculated via deformation potential theory, using Eqs. (2) – (5) in conjunction with the data of Table I. Solid (dashed) green lines show the direct band gap between Γ_7^- CB and HH- (LH-) like Γ_8^+ VB states. Solid (dashed) red lines show the indirect band gap between L_6^+ CB and HH- (LH-) like Γ_8^+ VB states. Closed blue triangles show the experimental measurements of Ref. 90.

morphic tensile strain can produce an indirect L_6^+-Γ_8^+ to direct Γ_7^--Γ_8^+ band gap transition – highlighted by the crossing of the dashed green and red lines in Fig. 6(a) – at in-plane tensile strain $\epsilon_{xx} \approx 1.4\%$. This transition is driven by a combination of (i) a downward shift of the Γ_7^- zone-centre CB edge energy due to the hydrostatic component of the pseudomorphic tensile strain (cf. Eq. (2)), and (ii) an upward shift in energy of the LH-like Γ_8^+ VB edge states due to the biaxial component of the pseudomorphic tensile strain (cf. Eq. (4)). We note that this is comparable to previous predictions of an indirect- to direct-gap transition for ϵ_{xx} in the range 1.5 – 1.9%.[37–39] For larger tensile strain, we observe further narrowing of the direct band gap, and predict that the band gap can be closed in Ge for tensile strain $\epsilon_{xx} \approx 4.4\%$. Under compressive strain we compute an increase (decrease) of the direct Γ_7^--Γ_8^+ (indirect L_6^+-Γ_8^+) band gap. Here, we emphasise that we are considering Ge under applied pseudomorphic strain. Under purely hydrostatic applied compression it would be expected that both the direct and direct band gaps increase in magnitude, as reflected by the negative values of the associated band gap hydrostatic deformation potentials (cf. Table I). Here, under compressive pseudomorphic strain, the upward energy shift of the HH-like Γ_8^+ VB edge states at fixed strain is larger than the upward energy shift of the L_6^+ CB edge states, leading to a net reduction of the indirect band gap.

Considering our calculated results for pristine α-Sn in Fig. 6(b), we note similar behaviour with good quantitative agreement between the TB-mBJ DFT- and deformation potential theory-calculated strain-dependent band gaps. We note, however, that while it would be expected that it should be possible to open the semimetallic (inverted) Γ_7^--Γ_8^+ energy gap under applied hydrostatic pressure, the splitting of the HH- and LH-like Γ_8^+ states in the presence of symmetry-breaking pseudomorphic strain prevents this. Specifically, we compute that the biaxial component of the pseudomorphic strain pushes the HH-like Γ_8^+ states higher in energy at a rate which is approximately equal to the upward energy shift of the Γ_7^- states due to the hydrostatic component of the strain. As such, the computed inverted direct band gap in Fig. 6(b) – closed green circles and solid green line – remains approximately constant as a function of compressive in-plane strain. Therefore, our calculations suggest that while it is in principle possible to close the energy band gap in highly tensile strained pseudomorphic Ge, it is not possible to open a band gap for realistic strain values in bulk-like α-Sn pseudomorphic strained layers.

Next, we investigate the strain-dependent band gaps of pseudomorphic $Ge_{1-x}Sn_x$ alloys grown on Ge, ZnTe and CdTe, and analyse how alloying and strain can be combined to engineer semiconducting or semimetallic epitaxial layers. Closed blue circles in Figs. 7(a), 7(b) and 7(c) respectively show the relevant DFT-calculated Γ_7^--Γ_8^+ energy gaps for pseudomorphically strained (a) $Ge_{1-x}Sn_x$/Ge, (b) $Ge_{1-x}Sn_x$/ZnTe and (c) $Ge_{1-x}Sn_x$/CdTe alloy SQSs. Results for $Ge_{1-x}Sn_x$/Ge are shown only for $x < 0.50$ as 64-atom SQSs having larger Sn compositions become amorphous when the ionic positions are allowed to relax.[36]

These DFT calculations are compared to deformation potential theory calculations in which the hydrostatic band gap deformation potential a_g is obtained via (i) linear interpolation between the values for Ge and α-Sn at each value of x (dashed red lines), or (ii) fitting to the results of the DFT calculations (solid black lines). In both cases, the VB edge axial deformation potential $b(\Gamma_8^+)$ for the alloy is determined by linear interpolation between the corresponding values for Ge and α-Sn (cf. Table I). The solid black lines in Figs. 7(a), 7(b) and 7(c) correspond to a best fit value $a_g(\Gamma_7^-\text{-}\Gamma_8^+) = -5.34$ eV, obtained by fitting to the DFT-calculated inverted direct energy gap of $Ge_{1-x}Sn_x$/ZnTe in Fig. 7(b). We note that this fitting is relatively insensitive to either Sn composition or choice of substrate, with similar values obtained by fitting to the DFT results for $Ge_{1-x}Sn_x$/Ge or $Ge_{1-x}Sn_x$/CdTe. We note that this composition-independent best-fit value

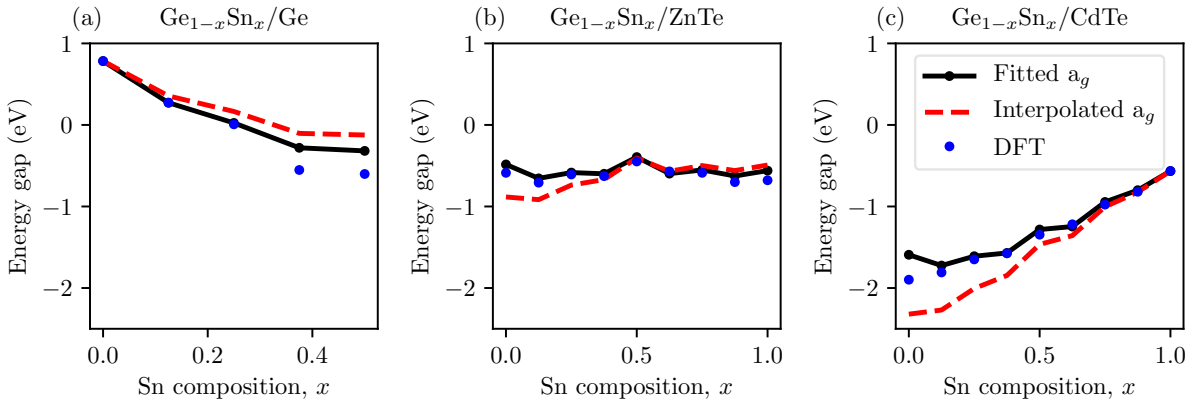

FIG. 7: Calculated Γ_7^--Γ_8^+ band gap as a function of Sn composition x, for pseudomorphically strained $Ge_{1-x}Sn_x$ SQSs grown on [001]-oriented (a) Ge, (b) ZnTe, and (c) CdTe substrates. Closed blue circles denote direct meta-GGA DFT calculations. Dashed red and solid black lines show the band gaps calculated using Eqs. (2) – (5), respectively employing a linearly interpolated and best-fit value for $a_g(\Gamma_7^-\text{-}\Gamma_8^+)$.

for $a_g(\Gamma_7^-\text{-}\Gamma_8^+)$ produces good quantitative agreement between the full DFT and model deformation potential calculations, tending only to break down in the presence of large in-plane strains $|\epsilon_{xx}| \gtrsim 5\%$ – i.e. at high and low x in Figs. 7(a) and 7(c) respectively – where linear-in-strain deformation potential theory is expected to lose accuracy.

The best-fit value $a_g = -5.34$ eV for the hydrostatic deformation potential associated with the $Ge_{1-x}Sn_x$ direct band gap is not intermediate between the values of -9.54 and -6.68 eV calculated respectively for the Γ_7^--Γ_8^+ band gaps of Ge and α-Sn (cf. Table I). This suggests that alloy-related band mixing effects play a key role in determining the nature of the band gap in $Ge_{1-x}Sn_x$ alloys, as the best fit value lies > 1 eV outside of the range expected from a virtual crystal-type linear interpolation which neglects potential band hybridisation. Indeed, our best-fit value for $a_g(\Gamma_7^-\text{-}\Gamma_8^+)$ is instead intermediate between the values associated with the direct Γ_7^--Γ_8^+ and indirect L_6^+-Γ_8^+ band gaps of Ge, reflecting that band folding in our 64-atom supercell calculations allows for hybridisation of Ge Γ- and L-point states in response to Sn incorporation. This is in agreement with recent theoretical analysis[40] suggesting that Sn incorporation in Ge drives strong hybridisation of Ge Γ- and L-point CB edge states, leading to a band gap that is neither purely indirect nor direct in nature, but which evolves continuously from having indirect to direct character via composition-dependent alloy band mixing. For $x \lesssim 0.10$ this conclusion is supported by pressure-dependent measurements,[52] which demonstrate that the pressure coefficient $\frac{dE_g}{dP}$ associated with the $Ge_{1-x}Sn_x$ fundamental band gap is that of the indirect L_6^+-Γ_8^+ Ge band gap at $x = 0$ (4.3 meV kbar^{-1}), and increases continuously with increasing x until it reaches a value close to that associated with the direct Γ_7^--Γ_8^+ band gap of Ge by $x \approx 0.10$ (12.9 meV kbar^{-1}). Converting our best-fit value $a_g = -5.34$ eV to a pressure coefficient (cf. Sec. II C) – via computation of the alloy bulk modulus based on interpolation of the elastic constants using the bowing parameters of Sec. II A – we indeed obtain an intermediate value $\frac{dE_g}{dP} \approx 7$ meV kbar^{-1}. We note that the limited band folding present in the $\lesssim 10^2$-atom supercells accessible using meta-GGA DFT calculations limits the number of states that can hybridise in response to alloying. As such, the observed Sn-induced Γ-L band mixing observed in our calculations persists across the entire composition range as an artefact of the supercells employed in our calculations, whereas experimental measurements suggest that alloy band mixing effects are most pronounced for $x \lesssim 0.10$. Indeed, we have recently described the presence of similar spurious hybridisation effects in alloy supercell calculations for $Ge_{1-x}Pb_x$ alloys.[91] Nonetheless, our calculations then support the emerging re-evaluation of the nature of the indirect- to direct-gap transition in $Ge_{1-x}Sn_x$ alloys in terms of alloy band mixing effects,[40,52] which have largely been neglected in previous analyses.

To compute the critical thickness t_c for $Ge_{1-x}Sn_x$ grown on Ge, ZnTe and CdTe substrates we use Eq. (6) with the DFT-calculated lattice and elastic constants listed in Table I. The results of these calculations are shown in Fig. 8 using solid red, dashed green and dash-dotted blue lines, respectively. Firstly, we calculate critical thicknesses at $|\epsilon_{xx}| = 1\%$ in order to provide guideline strain-thickness limit estimations. Our estimated strain-thickness limits are, respectively, $t_c \times |\epsilon_{xx}| = 22.8$ nm % and 24.4 nm % for $Ge_{1-x}Sn_x$ grown on Ge and CdTe. For $Ge_{1-x}Sn_x$/ZnTe, which is under compressive (tensile) in-plane strain for $x \gtrsim 0.54$ ($x \lesssim 0.54$), we estimate a strain-thickness limit $t_c \times |\epsilon_{xx}| = 23.3$ nm % (23.5 nm %). To compare the different substrates we choose a reference critical thickness of 5 nm, as a representative thickness along [001] of a thin film in which

quantum confinement effects can open a band gap in semimetallic $Ge_{1-x}Sn_x$. For $Ge_{1-x}Sn_x$/Ge we compute that the critical thickness reduces to 5 nm for Sn composition $x = 0.234$, corresponding to an in-plane compressive strain of magnitude $|\epsilon_{xx}| = 3.4\%$. In previous analysis,[36] we predicted based on LDA-calculated SQS total energies that it is energetically favourable for $Ge_{1-x}Sn_x$ to become amorphous for $x \gtrsim 0.56$. The calculations of Ref. 36 were performed for the same 64-atom SQSs considered in this work: these $2 \times 2 \times 2$ simple cubic supercells have a thickness of $2 \times a(x) = 1.2$ nm, where $a(x)$ is the relaxed alloy lattice constant along [001]. Indeed, we calculate $t_c \leq 2\,a(x)$ for $x \geq 0.566$. This excellent quantitative agreement between DFT alloy SQS total energy calculations and the critical thickness computed via Eq. (6) provides confidence in our predicted strain-thickness limits for $Ge_{1-x}Sn_x$. We also compare our calculated $Ge_{1-x}Sn_x$/Ge critical thickness to data of Suzuki et al.[35] (closed red circles in Fig. 8), which were estimated based on structural characterisation of $Ge_{1-x}Sn_x$/Ge epitaxial layers and measured elastic constants for Ge and α-Sn. While our calculations slightly underestimate the values of t_c estimated by Suzuki et al.[35], we note otherwise excellent qualitative agreement across the composition range for which data are available. For $Ge_{1-x}Sn_x$/ZnTe we compute that t_c is reduced to 5 nm for $x = 0.334$ ($x = 0.808$), corresponding to a tensile (compressive) in-plane strain of magnitude $|\epsilon_{xx}| = 3.1\%$ ($|\epsilon_{xx}| = 3.4\%$). Finally, for tensile strained $Ge_{1-x}Sn_x$/CdTe we compute $t_c = 5$ nm for $x = 0.759$, corresponding to a tensile in-plane strain of magnitude $|\epsilon_{xx}| = 2.8\%$. We therefore note that growing $Ge_{1-x}Sn_x$ on these three substrates allows $t_c \geq 5$ nm to be achieved across almost the entire composition range, with the exclusion of a gap for $0.234 \leq x \leq 0.334$, corresponding to relaxed lattice constants in the range $a(x) \approx 5.84$ – 5.92 Å.

We are now in a position to consider quantitatively the implications of the electronic structure and critical thickness for engineering the semimetal-to-semiconductor transition for the three substrates considered in this work. Growth of $Ge_{1-x}Sn_x$ on CdTe substrates increases the magnitude of the inverted Γ_7^--Γ_8^+ energy gap with decreasing x (cf. Fig. 5). This, combined with the associated reduction in critical thickness (cf. Fig. 8), suggests that growth of $Ge_{1-x}Sn_x$ on substrates having lattice constant close to that of α-Sn is not a suitable approach to produce semimetallic thin films in which a band gap could be opened below a given film thickness. Pseudomorphic growth of $Ge_{1-x}Sn_x$ on Ge requires Sn composition $x \gtrsim 0.26$ to close the alloy band gap and achieve a semimetallic alloy, compared to $x \approx 0.21$ in a relaxed alloy. In this composition range, we compute $Ge_{1-x}Sn_x$/Ge critical thickness $t_c \lesssim 5$ nm, suggesting that it is challenging to grow sufficiently thick defect-free films in order to achieve semimetallic materials, and hence the film would be semiconducting for the film thicknesses that could be achieved, preventing band gap modulation via variation of the film thickness. Finally, growth of $Ge_{1-x}Sn_x$ on a ZnTe substrate having a lattice constant intermediate between Ge and α-Sn produces an inverted-gap semimetallic alloy, with the magnitude of the inverted energy gap being relatively insensitive to Sn composition x. This stability of the inverted band gap with Sn composition x for $Ge_{1-x}Sn_x$/ZnTe could allow pseudomorphic growth of alloys having Sn composition close to lattice-matching to a ZnTe substrate for $x = 0.54$. As such, growth of $Ge_{1-x}Sn_x$ on ZnTe provides a route to circumvent critical thickness limitations simultaneously allowing, at fixed Sn composition, for growth of films having thicker semimetallic and thinner semiconducting regions. Our calculations suggest that $Ge_{1-x}Sn_x$/ZnTe layers have $t_c > 10$ nm for $0.42 \lesssim x \lesssim 0.69$, with the lower end of this composition range being more favourable for epitaxial growth in order to mitigate deleterious Sn segregation arising due to reduced alloy miscibility at higher Sn compositions.[35,36,92]

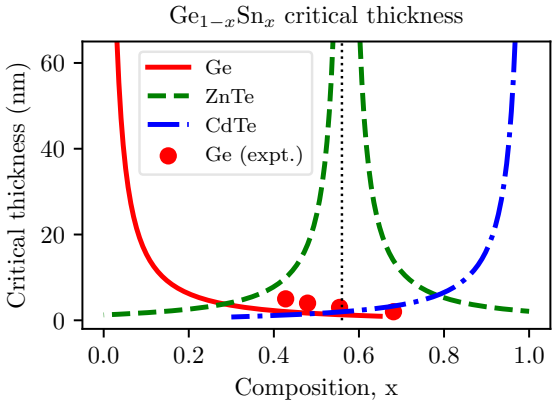

FIG. 8: Calculated Sn composition-dependent critical thickness t_c of pseudomorphically strained $Ge_{1-x}Sn_x$ grown on [001]-oriented Ge (solid red line), ZnTe (dashed green line), or CdTe (dash-dotted blue line) substrates. Closed red circles denote the critical thicknesses inferred in Ref. 35 based on structural characterisation of $Ge_{1-x}Sn_x$/Ge epitaxial layers.

Growth of $Ge_{1-x}Sn_x$/ZnTe having Sn compositions $x \gtrsim 0.42$ is demanding from the perspective of epitaxial growth. As such, it is also of interest to quantify the degree to which tensile strain can be exploited to lower the minimum Sn composition at which the alloy becomes semimetallic. This is similar in spirit to recent work on low x prototype $Ge_{1-x}Sn_x$ lasers, where Sn incorporation and tensile strain are simultaneously employed to drive the emergence of a direct band gap.[93] Reducing Sn composition reduces Sn segregation during growth, and promotes enhanced crystalline quality by enabling higher temperature growth. However, reduction in Sn composition at fixed strain will increase the magnitude of the band gap in the semiconducting regime. Application of tensile strain to reduce the band gap also reduces the critical thickness, leading to a trade-off for epitaxial growth of semimetallic $Ge_{1-x}Sn_x$. In practice, simultaneous in-

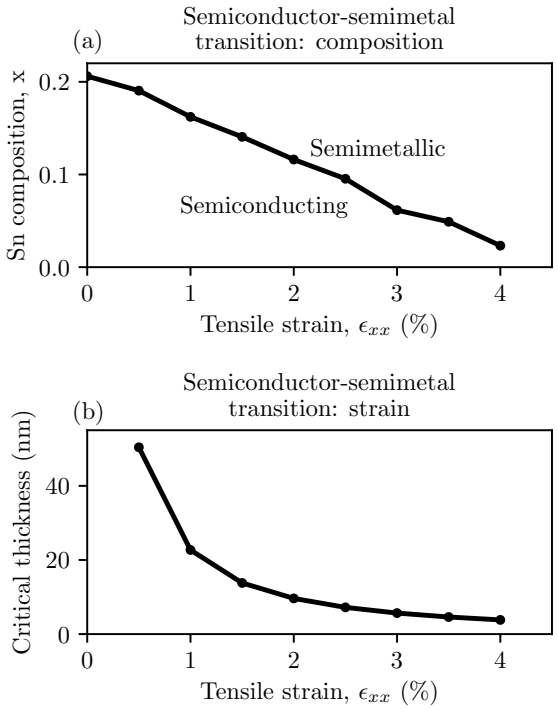

FIG. 9: (a) Sn composition x at which the band gap of [001]-oriented pseudomorphic $Ge_{1-x}Sn_x$ closes – i.e. the alloy becomes semimetallic – as a function of in-plane tensile strain ϵ_{xx}, demonstrating that the Sn composition required to close the alloy band gap can be strongly reduced via choice of substrate. (b) Critical thickness associated with the alloy Sn compositions of (a).

troduction of tensile strain and a reduction of Sn composition required to close the band gap can be achieved via growth on substrates having lattice constant intermediate between those associated with the relaxed $Ge_{1-x}Sn_x$ alloy and ZnTe.

We have calculated the minimum Sn composition at which the alloy becomes semimetallic as a function of applied tensile pseudomorphic strain for the same SQSs considered above. The results of these calculations are summarised in Figs. 9(a) and 9(b) which show, as a function of in-plane tensile strain, (a) the Sn composition x at which the alloy band gap closes, and (b) the critical thickness t_c corresponding to the Sn composition and tensile strain in (a). Figure 9(a) therefore summarises as a function of Sn composition and tensile strain the conditions under which pseudomorphic $Ge_{1-x}Sn_x$ alloys are predicted to be semiconducting or semimetallic. At zero strain, corresponding to the relaxed alloy calculations of Fig. 4, we recall that $x \approx 0.21$ is required to close the alloy band gap. The Sn composition at which the band gap closes is calculated to decrease approximately linearly with applied tensile strain, by $\approx 4.6\%$ Sn per % tensile strain (i.e. in-plane lattice mismatch ϵ_{xx}). We note that extrapolation to $x = 0$ in Fig. 9(a) gives $\epsilon_{xx} \approx 4.4\%$, corresponding to the closing of the direct band gap of Ge under pseudomorphic tensile strain (cf. Fig. 6(a)). Examining Fig. 9(b) we find $t_c \gtrsim 10$ nm for $\epsilon_{xx} \lesssim 2\%$, corresponding in Fig. 9(a) to Sn compositions $x \gtrsim 0.11$. As such, we predict that the minimum Sn composition required to close the alloy band gap can be reduced by a factor of approximately two in a tensile strained pseudomorphic $Ge_{1-x}Sn_x$ layer compared to a relaxed alloy, assuming that the layer is sufficiently thick to prevent opening of a band gap via quantum confinement.

The strained lattice constants of Figs. 9(a) and 9(b) lie in the range 5.80 – 5.89 Å, lower than the lattice constant of ZnTe. This suggests additional paths to engineer the minimum Sn composition at which the alloy becomes semimetallic: pseudomorphic growth of $Ge_{1-x}Sn_x$ on InP substrates, or metamorphic growth on relaxed $In_yGa_{1-y}As$ metamorphic buffer layers.[87] InP has a lattice constant of 5.87 Å,[94] lying within the range described above. $In_yGa_{1-y}As$ has a lattice constant varying between 5.65 Å ($y = 0$) and 6.06 Å ($y = 1$),[95] which covers the entire range described above, allowing for lattice matching to relaxed $Ge_{1-x}Sn_x$ alloys up to $x \approx 0.50$. Finally, Figs. 5 and 8 also suggest an alternative strategy for producing $Ge_{1-x}Sn_x$ thin films to engineer a semimetal-to-semiconductor transition by varying alloy film thickness. Pseudomorphic growth of a sufficiently thick, low x $Ge_{1-x}Sn_x$/Ge metamorphic buffer layer would exhibit semiconducting behaviour. Grown sufficiently thick to allow for relaxation, such a layer will possess an increased lattice constant relative to the Ge substrate. Subsequent growth on top of this buffer layer with increased x will increase the critical thickness relative to $Ge_{1-x}Sn_x$/Ge, pushing a given critical thickness to higher x. In this manner, thicker semimetallic $Ge_{1-x}Sn_x$ films grown on a lower x metamorphic buffer may be achievable. Alternatively, thinner unrelaxed buffer layers with increased x would also be suitable, as compressive strain and quantum confinement contribute to opening a band gap, allowing for a semiconducting virtual substrate. With a reduced band gap relative to the Ge substrate and buffer layer, electrical measurements can indicate if a semimetal-to-semiconductor transition can be achieved using such a growth scheme.

IV. CONCLUSIONS

In summary, we have presented a theoretical analysis of the electronic structure of $Ge_{1-x}Sn_x$ across the full alloy composition range. Using DFT calculations for SQS alloy supercells we have quantified the nature and evolution of the band gap of free-standing and pseudomorphically strained $Ge_{1-x}Sn_x$ with Sn composition x, and interpreted the electronic structure via (i) direct quantitative analysis of key alloy eigenstates, and (ii) model analysis based on deformation potential theory. Based on parameters extracted from DFT calculations, we additionally employed continuum elasticity theory to pro-

vide estimates of critical thickness limits associated with pseudomorphic growth of $Ge_{1-x}Sn_x$ epitaxial layers on Ge, ZnTe and CdTe substrates (with ZnTe and CdTe chosen for having lattice constant respectively close to that of zb-GeSn and α-Sn). The results of our electronic structure calculations were found to be in good quantitative agreement with experimental measurements across the range of Sn compositions for which data are currently available. Furthermore, our predicted critical thickness limits for pseudomorphically strained $Ge_{1-x}Sn_x$ alloys were found to be in quantitative agreement with the results of our first principles analysis of thermodynamic stability in $Ge_{1-x}Sn_x$,[36] predicting that it is energetically favourable for epitaxial $Ge_{1-x}Sn_x$/Ge layers to become amorphous for $x \gtrsim 0.56$.

In the low Sn composition range $x \lesssim 0.10$, our results firstly confirmed the presence of an indirect- to direct-gap transition, as described widely in the literature. The calculated values of the hydrostatic deformation potential (pressure coefficient) associated with the fundamental alloy band gap in this composition range were found to be intermediate between those associated with the indirect fundamental L_6^+-Γ_8^+, and direct Γ_7^--Γ_8^+ band gaps of Ge. This supports emerging evidence suggesting that Sn-induced hybridisation of Ge CB states plays a key role in characterising the indirect to direct-gap transition, which will have significant consequences for properties relevant to proposed device applications at low x. For $x \gtrsim 0.10$ we demonstrated that the minimum Sn composition required to close the alloy band gap can be engineered via both alloying and pseudomorphic strain. We predict that free-standing $Ge_{1-x}Sn_x$ becomes semimetallic at $x \approx 0.21$, and that combining alloying of Ge and Sn with strain engineering allows to significantly reduce the magnitude of the inverted (negative) Γ_7^--Γ_8^+ energy that must be overcome by quantum confinement to open a band gap in semimetallic $Ge_{1-x}Sn_x$. For tensile strained pseudomorphic $Ge_{1-x}Sn_x$, we estimate that the Sn composition required to reduce the inverted Γ_7^--Γ_8^+ energy separation can be reduced to $x \approx 0.11$ in $Ge_{1-x}Sn_x$ pseudomorphic layers having critical thickness $t_c \approx 10$ nm.

The realisation of recently proposed nanoscale intrinsic, confinement-modulated-gap diodes and transistors relies on the availability of materials for which the semimetal-to-semiconductor transition can be engineered to create thicker semimetallic regions adjacent to thinner semiconducting regions. In this respect, $Ge_{1-x}Sn_x$ alloys offer opportunities to engineer the electronic structure to meet novel device requirements. One advantage is the reduction of the magnitude of the inverted semimetallic energy gap to be overcome by quantum confinement in order to induce a band gap in semimetallic $Ge_{1-x}Sn_x$, compared to that in α-Sn. Reducing this inverted energy gap relaxes constraints on the minimum film thickness at which the semimetal-to-semiconductor transition can be observed. The possibility to explore pseudomorphic growth on different substrates and metamorphic buffer layers provides opportunities to combine alloy composition and strain engineering to control the Sn composition at which $Ge_{1-x}Sn_x$ becomes semimetallic. We note that further possibilities for band gap engineering in thin films and nanowires are also offered by, e.g., choice of surface termination, making $Ge_{1-x}Sn_x$ nanostructures a promising platform for electronics applications. Overall, we conclude that combining pseudomorphic strain with alloying in $Ge_{1-x}Sn_x$ presents rich opportunities for band structure engineering, presenting opportunities for novel applications in electronic and photonic devices at higher Sn compositions.

Acknowledgments

This work was supported by Science Foundation Ireland (SFI; project nos. 13/IA/1956 and 15/IA/3082), by the National University of Ireland (NUI; via the Post-Doctoral Fellowship in the Sciences, held by C.A.B.), with partial support from the Nottingham-Ningbo Materials Institute and National Natural Science Foundation of China with a project code 61974079.

* Electronic address: c.broderick@umail.ucc.ie
† Electronic address: jim.greer@nottingham.edu.cn

[1] C. Darmody, D. P. Ettisserry, N. Goldsman, and N. K. Dhar, in *International Conference on Simulation of Semiconductor Processes and Devices (SISPAD)* (2015).
[2] J. D. Sau and M. L. Cohen, Phys. Rev. B **75**, 045208 (2007).
[3] B. Dutt, H. Lin, D. S. Sukhdeo, B. M. Vulović, S. Gupta, D. Nam, K. C. Saraswat, and J. S. Harris, IEEE J. Sel. Top. Quantum Electron. **19**, 1502706 (2013).
[4] K. L. Low, Y. Yang, G. Han, W. Fan, and Y.-C. Yeo, J. Appl. Phys. **112**, 103715 (2012).
[5] J. Doherty, S. Biswas, E. Galluccio, C. A. Broderick, A. Garcia-Gil, R. Duffy, E. P. O'Reilly, and J. D. Holmes, Chem. Mater. **32**, 4383 (2020).
[6] K. P. Homewood and M. A. Lourenço, Nature Photonics **9**, 78 (2015).
[7] S. Wirths, R. Geiger, N. von den Driesch, G. Mussler, T. Stoica, S. Mantl, Z. Ikonic, M. Luysberg, S. Chiussi, J. M. Hartmann, et al., Nature Photonics **9**, 88 (2015).
[8] E. Kasper and M. Oehme, Jpn. J. Appl. Phys. **54**, 04DG11 (2015).
[9] Y. Yang, S. Su, P. Guo, W. Wang, X. Gong, L. Wang, K. L. Low, G. Zhang, C. Xue, B. Cheng, et al., in *IEEE International Electron Devices Meeting (IEEE-IEDM)* (2012).
[10] L. Liu, R. Liang, J. Wang, L. Xiao, and J. Xu, Appl. Phys. Express **9**, 091301 (2016).
[11] S. Sant and A. Schenk, IEEE J. Electron Devices Soc. **3**, 164 (2015).
[12] M. D. Dunne, C. A. Broderick, M. Luisier, and E. P.

O'Reilly, in *International Conference on Numerical Simulation of Optoelectronic Devices (NUSOD)* (2020).
[13] P. Moontragoon, Z. Ikonić, and P. Harrison, Semicond. Sci. Technol. **22**, 742 (2007).
[14] D. W. Jenkins and J. D. Dow, Phys. Rev. B **36**, 7994 (1987).
[15] M. P. Polak, P. Scharoch, and R. Kudrawiec, journal of Physics D: Applied Physics **50**, 195103 (2017).
[16] L. Ansari, G. Fagas, J.-P. Colinge, and J. C. Greer, Nano Lett. **12**, 2222 (2012).
[17] J. P. Colinge and J. C. Greer, *Nanowire Transistors: Physics of Devices and Materials in One Dimension* (Cambridge University Press, Cambridge, 2016), ISBN 9781107280779.
[18] H. Da, K. Lam, G. Samudra, S. Chin, and G. Liang, IEEE Tran. Electron. Dev. **59**, 1454 (2012).
[19] A. Sanchez-Soares and J. C. Greer, Nano Lett. **16**, 7639 (2016).
[20] F. Gity, L. Ansari, M. Lanius, P. Schüffelgen, G. Mussler, D. Grützmacher, and J. C. Greer, Appl. Phys. Lett. **110**, 093111 (2017).
[21] F. Gity, L. Ansari, C. König, G. A. Verni, J. D. Holmes, B. Long, M. Lanius, P. Schüffelgen, G. Mussler, D. Grützmacher, et al., Microelectron. Eng. **195**, 21 (2018).
[22] J. C. Greer, A. Blom, and L. Ansari, J. Phys.: Condens. Matter **30**, 414003 (2018).
[23] E. Cohen and A. K. W. A. van Lieshout, Z. Phys. Chem. (N. F.) **173A** (1935).
[24] K. Houben, J. K. Jochum, D. P. Lozano, M. Bisht, E. Menéndez, D. G. Merkel, R. Rüffer, A. I. Chumakov, S. Roelants, B. Partoens, et al., Phys. Rev. B **100**, 075408 (2019).
[25] R. F. C. Farrow, D. S. Robertson, G. M. Williams, A. G. Cullis, G. R. Jones, I. M. Young, and P. N. J. Dennis, J. Cryst. Growth **54**, 507 (1981).
[26] R. C. Bowman, P. M. Adams, M. A. Engelhart, and H. Höchst, J. Vac. Sci. Technol. A **8**, 1577 (1990).
[27] S. Groves and W. Paul, Phys. Rev. Lett. **11**, 194 (1963).
[28] S. Küfner, J. Furthmüller, L. Matthes, M. Fitzner, and F. Bechstedt, Phys. Rev. B **87**, 235307 (2013).
[29] H.-S. Lan, S. T. Chang, and C. W. Liu, Phys. Rev. B **95**, 201201 (2017).
[30] A. W. Ewald, J. Appl. Phys. **25**, 1436 (1954).
[31] R. W. Olesinski and G. J. Abbaschian, Bull. Alloy Phase. Diagr. **5**, 265 (1984).
[32] J. Piao, R. Beresford, T. Licata, W. I. Wang, and H. Homma, J. Vac. Sci. Technol. B **8**, 221 (1990).
[33] G. He and H. A. Atwater, Appl. Phys. Lett. **68**, 664 (1996).
[34] S. Biswas, J. Doherty, D. Saladukha, Q. Ramasse, D. Majumdar, M. Upmanyu, A. Singha, T. Ochalski, M. A. Morris, and J. D. Holmes, Nature Communications **7**, 11405 (2016).
[35] A. Suzuki, O. Nakatsuka, S. Shibayama, M. Sakashita, W. Takeuchi, M. Kurosawa, and S. Zaima, Jpn. J. Appl. Phys. **55**, 04EB12 (2016).
[36] A. Sanchez-Soares, C. O'Donnell, and J. C. Greer, arXiv:1904.09147 (2019), URL `http://arxiv.org/abs/1904.09147`.
[37] S. Gupta, B. Magyari-Köpe, Y. Nishi, and K. C. Saraswat, J. Appl. Phys. **113**, 073707 (2013).
[38] M. Virgilio, C. L. Manganelli, G. Grosso, G. Pizzi, and G. Capellini, Phys. Rev. B **87**, 235313 (2013).
[39] M. E. Kurdi, G. Fishman, S. Sauvage, and P. Boucaud, J. Appl. Phys. **107**, 013710 (2010).
[40] E. J. O'Halloran, C. A. Broderick, D. S. P. Tanner, S. Schulz, and E. P. O'Reilly, Opt. Quantum Electron. **51**, 314 (2019).
[41] D. S. P. Tanner, C. A. Broderick, A. C. Kirwan, S. Schulz, and E. P. O'Reilly, "Fully analytic valence force fields for the relaxation of group-IV semiconductor alloys: elastic properties of group-IV materials calculated from first principles", submitted (2020).
[42] E. K. U. Dreizler, Reiner M. and Gross, in *Density Functional Theory* (Springer, 1990), ISBN 978-3-642-86107-9.
[43] J. P. Perdew and A. Zunger, Phys. Rev. B **23**, 5048 (1981).
[44] F. Tran and P. Blaha, Phys. Rev. Lett. **102**, 226401 (2009).
[45] J. M. Soler, E. Artacho, J. D. Gale, A. García, J. Junquera, P. Ordejón, and D. Sánchez-Portal, J. Phys.: Condens. Matter **14**, 2745 (2002).
[46] T. Ozaki, Phys. Rev. B **67**, 155108 (2003).
[47] T. Ozaki and H. Kino, Phys. Rev. B **69**, 195113 (2004).
[48] H. J. Monkhorst and J. D. Pack, Phys. Rev. B **13**, 5188 (1976).
[49] C. Eckhardt, K. Hummer, and G. Kresse, Phys. Rev. B **89**, 165201 (2014).
[50] M. Råsander and M. A. Moram, J. Chem. Phys. **143**, 144104 (2015).
[51] S.-H. Wei and A. Zunger, Phys. Rev. B **60**, 5404 (1999).
[52] T. D. Eales, I. P. Marko, S. Schulz, E. O'Halloran, S. Ghetmiri, W. Du, Y. Zhou, S.-Q. Yu, J. Margetis, J. Tolle, et al., Sci. Rep. **9**, 14077 (2019).
[53] M. Cardona, J. Phys. Chem. Solids **17**, 138 (1960).
[54] B. Welber, M. Cardona, Y.-F. Tsay, and B. Bendow, Phys. Rev. B **15**, 875 (1977).
[55] A. R. Goni, K. Syassen, K. Strossner, and M. Cardona, Semicond. Sci. Technol. **4**, 246 (1989).
[56] J. F. C. Baker and M. Hart, Acta Crystallogr. A **31**, 364 (1975).
[57] J. Thewlis and A. R. Davey, Nature **174**, 1011 (1954).
[58] H. J. McSkimin and P. Andreatch, J. Appl. Phys. **34**, 651 (1963).
[59] D. L. Price, J. M. Rowe, and R. M. Nicklow, Phys. Rev. B **3**, 1268 (1971).
[60] S.-G. Shen, J. Phys.: Condens. Matter **6**, 8733 (1994).
[61] H. B. Huntington, in *Solid State Physics* (Elsevier, 1958), vol. 7, pp. 213–351.
[62] A. D. Zdetsis, J. Phys. Chem. Solids **38**, 1113 (1977).
[63] S. Zwerdling, B. Lax, L. M. Roth, and K. J. Button, Phys. Rev. **114**, 80 (1959).
[64] B. L. Booth and A. W. Ewald, Phys. Rev. **168**, 796 (1968).
[65] S. Wirths, D. Buca, and S. Mantl, Prog. Cryst. Growth Charact. Mater. **62**, 1 (2016).
[66] S. H. Groves, C. R. Pidgeon, A. W. Ewald, and R. J. Wagner, J. Phys. Chem. Solids **31**, 2031 (1970).
[67] A. Qteish and R. J. Needs, Phys. Rev. B **45**, 1317 (1992).
[68] C. Rödl, J. Furthmüller, J. R. Suckert, V. Armuzza, F. Bechstedt, and S. Botti, Phys. Rev. Materials **3**, 034602 (2019).
[69] O. Madelung and U. Rössler, *Group-IV Elements, IV-IV and III-V Compounds. Part b - Electronic, Transport, Optical and Other Properties* (Springer, Heidelberg, 2002).
[70] C. G. V. de Walle, Phys. Rev. B **39**, 1871 (1989).
[71] M. V. Fischetti and S. E. Laux, J. Appl. Phys. **80**, 2234 (1996).
[72] B. J. Roman and A. W. Ewald, Phys. Rev. B **5**, 3914 (1972).
[73] A. Zunger, S. H. Wei, L. G. Ferreira, and J. E. Bernard,

Phys. Rev. Lett. **65**, 353 (1990).
[74] K. C. Hass, L. C. Davis, and A. Zunger, Phys. Rev. B **42**, 3757 (1990).
[75] A. V. D. Walle, M. Asta, and G. Ceder, Calphad **26**, 539 (2002).
[76] M. P. C. M. Krijn, Semicond. Sci. Technol. **6**, 27 (1991).
[77] M. Usman, C. A. Broderick, and E. P. O'Reilly, Phys. Rev. Applied **10**, 044024 (2018).
[78] M. Usman, C. A. Broderick, Z. Batool, K. Hild, T. J. C. Hosea, S. J. Sweeney, and E. P. O'Reilly, Phys. Rev. B **87**, 115104 (2013).
[79] S. Schulz, C. A. Broderick, E. J. O'Halloran, and E. P. O'Reilly, in *International Conference on Numerical Simulation of Optoelectronic Devices (NUSOD)* (2018), pp. 39–40.
[80] M. A. Caro, S. Schulz, and E. P. O'Reilly, J. Phys.: Condens. Matter **25**, 025803 (2012).
[81] E. P. O'Reilly, Semicond. Sci. Technol. **4**, 121 (1989).
[82] P. Voisin, in *Quantum Wells and Superlattices in Optoelectronic Devices and Integrated Optics* (1988), vol. 861, pp. 88–96.
[83] S. Tomić and E. P. O'Reilly, IEEE Photo. Tech. Lett. **15**, 6 (2003).
[84] C. A. Broderick, S. R. Jin, I. P. Marko, K. Hild, P. Ludewig, Z. L. Bushell, W. Stolz, J. M. Rorison, E. P. O'Reilly, K. Volz, et al., Sci. Rep. **7**, 46371 (2017).
[85] A. Sanchez-Soares, C. O'Donnell, and J. C. Greer, Phys. Rev. B **94**, 235442 (2016).
[86] J. M. Sanchez, F. Ducastelle, and D. Gratias, Physica A **128**, 334 (1984).
[87] H. Lin, R. Chen, W. Lu, Y. Huo, T. Kamins, and J. S. Harris, Appl. Phys. Lett. **100**, 102109 (2012).
[88] H. Tran, W. Du, S. A. Ghetmiri, A. Mosleh, G. Sun, R. A. Soref, J. Margetis, J. Tolle, B. Li, H. A. Naseem, et al., J. Appl. Phys. **119**, 103106 (2016).
[89] C. Xu, P. M. Wallace, D. A. Ringwala, S. L. Y. Chang, C. D. Poweleit, J. Kouvetakis, and J. Menéndez, Appl. Phys. Lett. **114**, 212104 (2019).
[90] M. E. Kurdi, H. Bertin, E. Martincic, M. D. Kersauson, G. Fishman, S. Sauvage, A. Bosseboeuf, and P. Boucaud, Appl. Phys. Lett. **96**, 041909 (2010).
[91] C. A. Broderick, E. J. O'Halloran, and E. P. O'Reilly, arXiv:1911.05679 (2019), URL `http://arxiv.org/abs/1911.05679`.
[92] T. Tsukamoto, N. Hirose, A. Kasamatsu, T. Mimura, T. Matsui, and Y. Suda, Appl. Phys. Lett. **106**, 052103 (2015).
[93] A. Elbaz, D. Buca, N. von den Driesch, K. Pantzas, G. Patriarche, N. Zerounian, E. Herth, X. Checoury, S. Sauvage, I. Sagnes, et al., Nature Photonics **14**, 375 (2020).
[94] I. Vurgaftman, J. R. Meyer, and L. R. Ram-Mohan, J. Appl. Phys. **89**, 5815 (2001).
[95] W. M. Haynes, *CRC Handbook of Chemistry and Physics, 95th Edition* (CRC Press, 2014), ISBN 978-1482208672.